Influence of Creep Compaction and Dilatancy on Earthquake Sequences and Slow Slip

Yuyun Yang[1,2], Eric M. Dunham[1,3]

[1]Institute for Computational and Mathematical Engineering, Stanford University
[2]Earth System Science Programme, Faculty of Science, The Chinese University of Hong Kong
[3]Department of Geophysics, Stanford University

Key Points:

- Fluid pressure changes from pore compaction and dilatancy influence slow slip events in our model
- Modeled slow slip events span long-term events lasting for months to years to rapid short-term events for a few days
- Earthquake recurrence interval is controlled in part by compaction-driven pressurization and weakening

1 Abstract

Fluids influence fault zone strength and the occurrence of earthquakes, slow slip events, and aseismic slip. We introduce an earthquake sequence model with fault zone fluid transport, accounting for elastic, viscous, and plastic porosity evolution, with permeability having a power-law dependence on porosity. Fluids, sourced at a constant rate below the seismogenic zone, ascend along the fault. While the modeling is done for a vertical strike-slip fault with 2D antiplane shear deformation, the general behavior and processes are anticipated to apply also to subduction zones. The model produces large earthquakes in the seismogenic zone, whose recurrence interval is controlled in part by compaction-driven pressurization and weakening. The model also produces a complex sequence of slow slip events (SSEs) beneath the seismogenic zone. The SSEs are initiated by compaction-driven pressurization and weakening and stalled by dilatant suctions. Modeled SSE sequences include long-term events lasting from a few months to years and very rapid short-term events lasting for only a few days; slip is $\sim$1-10 cm. Despite $\sim$1-10 MPa pore pressure changes, porosity and permeability changes are small and hence fluid flux is relatively constant except in the immediate vicinity of slip fronts. This contrasts with alternative fault valving models that feature much larger changes in permeability from the evolution of pore connectivity. Our model demonstrates the important role that compaction and dilatancy have on fluid pressure and fault slip, with possible relevance to slow slip events in subduction zones and elsewhere.

Plain Language Summary

Water in the crust plays an important role in controlling the strength of fault zones and frictional sliding, which manifest as earthquakes and slow slip events that do not produce ground shaking. In this study, we perform computer modeling of earthquake sequences that are coupled to the evolution of fluid pressure and rock properties. In particular, compaction or dilation of the water-filled pore space in rock drives changes in fluid pressure and influences the fault's frictional resistance to slip. The model quantifies the effects of compaction and dilation on both large earthquakes and slow slip events,

---

Corresponding author: Yuyun Yang, `yuyunyang@cuhk.edu.hk`

providing specific predictions regarding slow slip event properties, pressure changes, and changes in fluid flow that might be testable with geophysical, geologic, and geochemical data.

2 Introduction

The role of fluids in controlling fault zone strength and the occurrence of earthquakes, slow slip events, and aseismic slip has been recognized for many decades. The focus on fluids has mounted in recent years as new observations are linking fluids to slow slip and possibly even the nucleation of great earthquakes (Saffer & Bekins, 1998; Ito et al., 2007; Frank et al., 2015; Khoshmanesh & Shirzaei, 2018; Ruiz & Madariaga, 2018; Warren-Smith et al., 2019; Gosselin et al., 2020; Sibson, 2020; Pritchard et al., 2020). Fluids are present throughout the seismogenic zone and below it, with much evidence for pore fluid pressures in excess of hydrostatic at depth. Fluid flow and pore pressure are also likely to be dynamic quantities, varying over coseismic to interseismic timescales, as a consequence of nonlinear coupling between slip and fluid transport properties like porosity and permeability (Sibson, 1992a).

The processes influencing fluid transport and its coupling to slip depend on the tectonic environment and the pressure-temperature conditions associated with different depths. In the seismogenic zone, fault slip is localized within a low permeability fault core, which is surrounded by a damage zone having elevated permeability and storage capacity (Caine et al., 1996; Faulkner et al., 2010). Fluids are preferentially channeled along faults, with along-fault transport occurring primarily within the damage zone. Cataclastic fault rocks are formed by fracturing and rotation of mineral grains and grain fragments accompanied by dilatancy and frictional sliding along grain boundaries (Woodcock & Mort, 2008). Low strain rate deformation can also occur through fluid-assisted diffusive mass transfer and pressure solution (Rutter, 1983; Renard et al., 2000; Fagereng & Toy, 2011; Gratier et al., 2013). Near the base of the seismogenic zone, which is the primary focus of our study, elevated temperatures activate other deformation mechanisms and chemical processes that influence fluid transport and pore pressure dynamics. We separate our discussion here by tectonic environment, briefly reviewing faults in both continental crust and subduction zones.

In the continental crust, deviatoric stresses decrease in the lower crust due to the onset of dislocation creep (Byerlee, 1978; Goetze & Evans, 1979; Brace & Kohlstedt, 1980; Poirier, 1985; Karato, 2008), sometimes also accompanied by fluid-assisted diffusive mass transfer and pressure solution (Rutter, 1983; Renard et al., 2000; Gratier et al., 2003; Fagereng & Toy, 2011; Gratier et al., 2013). Deformation is distributed across a broader shear zone (Molnar et al., 1999; Norris & Cooper, 2003; Fossen & Cavalcante, 2017), though there is also much evidence for a transitional region exhibiting both localized frictional shear and distributed deformation (Cole et al., 2007; Frost et al., 2011; Kirkpatrick & Rowe, 2013). Fluids are channeled upward along faults, with fluid sources including meteoric water, mantle-derived fluid, and fluids released during metamorphic dehydration reactions (Kennedy et al., 1997; Faulkner & Rutter, 2001; Fulton & Saffer, 2009; Menzies et al., 2016). In certain locations, such as the central section of the San Andreas Fault, fluids are also sourced by dehydration reactions within paleo-subduction rocks (Bürgmann, 2018). Tremor and slow earthquakes occur in the lower crust below the seismogenic zone, at depths of $\sim$15-30 km, on the San Andreas Fault near Parkfield (Shelly & Hardebeck, 2010; Rousset et al., 2019). Correlations between tremor and tidal forcing provide evidence for low effective normal stress and near-lithostatic pore fluid pressures.

Fluids are arguably even more important in subduction zones. In the shallow accretionary prism, mechanical compaction of subducting sediments creates overpressure (Saffer & Tobin, 2011), which many have linked to shallow slow slip events (Saffer & Wallace, 2015; Araki et al., 2017; Bürgmann, 2018). At greater depths, near and below the base of the seismogenic zone, increasing temperatures and pressures activate various dehydration reactions (Hyndman & Peacock, 2003; Hacker et al., 2003; Peacock, 2009; Fagereng & Diener, 2011; Condit et al., 2020). Fluids can also be sourced by volatile release from the mantle (Kerrick & Connolly, 2001). Slow slip and tremor at these depths are widespread across many subduction zones (Schwartz & Rokosky, 2007; Beroza & Ide, 2011; Bürgmann, 2018) and fluid pressures are again thought to be close to lithostatic (Schwartz & Rokosky, 2007; Audet et al., 2009; Peacock et al., 2011; Saffer & Wallace, 2015; Condit & French, 2022). Fault structure and deformation is complex as a consequence of the compositional, and hence rheological, heterogeneity and layering within the subducting oceanic crust and overriding plate (Behr & Bürgmann, 2021; Kirkpatrick et al., 2021).

The goal of our work is to quantitatively explore controls on fault zone fluid transport, pore pressure evolution, and their coupling to fault slip using the modern framework of earthquake sequence modeling. While this is done in the context of a vertical strike-slip fault model, described subsequently, we anticipate than many of the general findings are applicable also to subduction zones. We are primarily concerned with the longer timescales relevant to slow earthquakes and earthquake cycle dynamics, for which along-fault fluid flow and pressure diffusion in fault damage zones are important. We assume pressure equilibration across the width of the fault zone, such that the pressure on slip surfaces within the fault core is approximately the same as the pressure within the damage zone. This is valid at timescales exceeding the hydraulic diffusion time across the fault zone width. For example, the diffusion time across 20 m is approximately 1 day for a hydraulic diffusivity of 10^{-3} m^2/s. Fault cores can have much lower diffusivity $\sim 10^{-6}$ m^2/s (Wibberley, 2002) and fault-normal pressure diffusion, over diffusion lengths $\sim 10^{-3}$ m, must be considered for shorter timescale processes such as thermal pressurization (Rice, 2006). We do not consider these processes and thus emphasize that the relevant fluid transport properties at longer timescales are those of the damage zone. We also assume that fluid sources are deeper than our region of interest, and that fluids are channeled upward along the fault zone, so the only relevant processes are those controlling porosity and permeability and hence fluid ascent.

The processes that we will study include changes in porosity from dilatancy and compaction. Porosity is one of the key controls on permeability, with permeability commonly assumed to have a power-law relation to porosity (Mavko et al., 2020). Dilatancy refers to inelastic opening of pore space through fracture and shearing, which if occurring under undrained conditions, creates a suction (reduction in pore pressure) that can stabilize against frictional slip and shearing. Compaction is the opposite, inelastic closure of pore space, and can occur through granular flow, closure of microcracks and fissures, and also as creep closure of pores from viscous flow of the matrix and chemical dissolution-precipitation processes. Changes in porosity can also be elastic, referring to reversible porosity changes caused by changes in effective normal stress. Dilatancy and compaction have been observed in many experiments involving shearing of fluid-saturated gouge and sliding of rough surfaces (Marone et al., 1990; Faulkner et al., 2018; Proctor et al., 2020; Brantut, 2020). Segall and Rice (1995) introduced a widely used model for dilatancy (and compaction) that has received much attention as a possible stabilizing mechanism to help explain slow earthquakes (Segall et al., 2010; Liu & Rubin, 2010; Segall & Bradley, 2012). Others have used similar models (Suzuki & Yamashita, 2009). The Segall and Rice (1995) model is inspired by models used in critical state soil mechanics (Wood, 1990) and is arguably most applicable to shearing of fault gouge. It is not obvious whether it is an appropriate model for dilatancy occurring within the damage zone and broader fault zone. Coseismic dilatancy in the damage zone during rupture propagation is likely controlled by the inelastic yielding that occurs during the passage of the stress concentration at the rupture front (Andrews, 2005; Templeton & Rice, 2008; Viesca et al., 2008). Slow earthquakes also feature stress concentrations at slip fronts so could conceivably activate dilatancy in a similar manner. The abundance of veins in exhumed rocks from the base of the seismogenic zone and at the depths of slow earthquakes

(Hickman et al., 1995; Behr & Bürgmann, 2021; Kirkpatrick et al., 2021) demonstrates that dilatancy is important at these greater depths, as well.

In addition to the compaction that is described by the Segall and Rice (1995) model, we also account for compaction by creep closure of pores by viscous flow of the matrix and/or fluid-mediated mass transfer processes. Viscous matrix flow occurs through the thermally activated deformation mechanisms discussed earlier, such as pressure solution, dislocation creep, and other crystal plastic flow mechanisms, and therefore becomes more important at depth where temperatures are higher. The closure of cracks and pores can also occur through chemical processes like the dissolution and precipitation of silica or other minerals, cementation, and crack healing (Hickman et al., 1995; Renard et al., 2000; Morrow et al., 2001; Gratier et al., 2003; Cox, 2005; Saishu et al., 2017; Williams & Fagereng, 2022). Compaction-driven pressurization and weakening of faults, which occurs on interseismic or even longer timescales, was proposed several decades ago (Walder & Nur, 1984; Nur & Walder, 1992; Sleep & Blanpied, 1992, 1994; Miller et al., 1996; Miller & Nur, 2000). Those authors explored, through early versions of earthquake sequence models, the occurrence of cycles of interseismic pressurization and weakening, coseismic enhancement of porosity and permeability, and postseismic depressurization from fluid discharge. These models captured many features that were observed geologically and explained in terms of fault valving (Sibson, 1992a). More recent studies have also examined creep compaction. Skarbek and Rempel (2016) introduced a fluid transport and pore pressure evolution model with porosity changes from dehydration reactions and creep compaction. Their model produces porosity waves whose periodicity bears similarity to the recurrence interval of slow slip events in subduction zones, though the model does not explicitly account for frictional slip. A similar model that also produces porosity waves was introduced by Yarushina et al. (2020), who performed a detailed study of the response of a fluid-filled pore to plastic and viscoplastic matrix deformation under combined pressure and shear loading.

Compaction, fault valving, and related topics are receiving renewed attention given recent advances in earthquake sequence modeling and observations of slow earthquakes and other fluid-related faulting phenomena. Petrini et al. (2020), Dal Zilio and Gerya (2022), and Dal Zilio, Hegyi, et al. (2022) utilized a geodynamic modeling approach, recently extended to earthquake sequences, to study the influence of fluids and pore pressure changes on shear localization, fault formation, and earthquake occurrence. Their models employ a poro-visco-elastic-plastic rheology with slip distributed across a finite width shear zone in which effective shear viscosity is reduced relative to the surrounding rock to mimic frictional sliding. This is in contrast to most other earthquake sequence models that idealize faults as frictional interfaces. Their models feature coseismic, rather than interseismic, compaction and pressurization. Pressurization-driven weakening, rather than frictional weakening, is the primary control on earthquake stress drop and rupture propagation. We return to these studies in the Discussion section, after having presented our model and results, to explain why their model and its predictions differ from ours and others in the literature.

Another earthquake sequence model accounting for fluid flow and pore pressure dynamics was introduced by Zhu et al. (2020) to study fault valving. Zhu et al. (2020) introduced an evolution equation for permeability, rather than porosity, with permeability increasing with slip and decreasing with time, the latter as a proxy for healing and sealing processes. The model produced fluid-driven aseismic slip events at the base of the seismogenic zone as well as swarm-like seismicity in the seismogenic zone, both occurring in concert with the ascent of a fluid overpressure pulse. Permeability changes of several orders of magnitude led to intermittent fluid flow, characteristic of fault valving. This model lacks dilatancy and the stabilizing effects of dilatant suctions, as a consequence of evolving permeability directly with porosity held fixed. It can be viewed as an end-member model accounting only for changes in permeability in response to changes in tortuosity or pore connectivity, rather than porosity itself. Our present study explores the opposite end-member model, in which permeability evolves only in response to changes in porosity. As we demonstrate below, this model does not produce fault valving, at least for the chosen parameters, but nonetheless generates pore pressure dynamics that have a fundamental influence on fault slip. Our model produces aseismic slip events akin to slow earthquakes, in fact with many similar features to the slow earthquakes in Zhu et al. (2020), but caused by a different mechanism. As the present time, it is unclear which model, if either, provides a better description of reality, and we provide suggestions in the Discussion section on experimental and geological studies that might help discriminate between these two end-member models.

3 Model

3.1 Elasticity and Friction

We utilize a model setup (Figure 1) similar to Allison and Dunham (2018) and Zhu et al. (2020) by considering the 2D antiplane shear problem of a planar, vertical strike-slip fault embedded in a linear elastic medium. The fault is located at $y = 0$, z measures depth with respect to the free surface at $z = 0$, and displacements $u(y, z, t)$ are in the x-direction. We exploit symmetry conditions about $y = 0$ and solve the elasticity problem only for one side of the fault ($y > 0$).

The governing equations for antiplane shear deformation are

$$\rho \frac{\partial^2 u}{\partial t^2} = \frac{\partial \sigma_{xy}}{\partial y} + \frac{\partial \sigma_{xz}}{\partial z}, \quad \sigma_{xy} = \mu \frac{\partial u}{\partial y}, \quad \sigma_{xz} = \mu \frac{\partial u}{\partial z}, \tag{1}$$

where σ_{xy} and σ_{xz} are the stress changes associated with displacement u, and ρ and μ are the density and shear modulus, which we assume are constant. Symmetry conditions allow us to define slip and slip velocity as

$$\delta(z, t) = 2u(0, z, t) \quad \text{and} \quad V(z, t) = \partial\delta/\partial t, \tag{2}$$

respectively. The fault boundary conditions are

$$\tau = f(\theta, V)\sigma', \tag{3}$$

$$\dot{\theta} = G(\theta, V), \tag{4}$$

where $\tau(z, t)$ is the shear stress, $\sigma'(z, t) = \sigma'_0(z) - p(z, t)$ is the effective normal stress where σ'_0 is the effective normal stress on the fault with hydrostatic pressure and p is the overpressure (the difference between pore pressure and hydrostatic pressure, $p_{\text{hydro}} = \rho_f g z$, where ρ_f is the fluid density and g is gravity). Equation (3) sets the shear stress equal to the frictional strength, where $f(\theta, V)$ is the rate-and-state friction coefficient and $\theta(z, t)$ is the state variable. Equation (4) is the state evolution equation.

We switch between the quasi-dynamic approximation with radiation damping (Rice, 1993) at low slip velocities (for which the radiation-damping term is effectively negligible) and a dynamic solver with full inertial effects at high slip velocities (Duru et al., 2019). In the quasi-dynamic approximation,

$$\tau(z, t) = \tau_0 + \sigma_{xy}(0, z, t) - \eta_{rad} V, \tag{5}$$

where τ_0 is the initial shear stress and $\eta_{rad} = \rho c/2$ is the radiation damping parameter with $c = \sqrt{\mu/\rho}$ being the S-wave speed. In the dynamic solver, we disable radiation damping. Switching between quasi-dynamic and fully dynamic solvers is based on the nondimensional ratio $R = \eta_{rad} V/\tau_{qs}$, where the numerator is the radiation damping term and the denominator is the quasi-static shear stress (Duru et al., 2019). We choose $R = 2 \times 10^{-4}$ to control switching into and out of the fully dynamic solver.

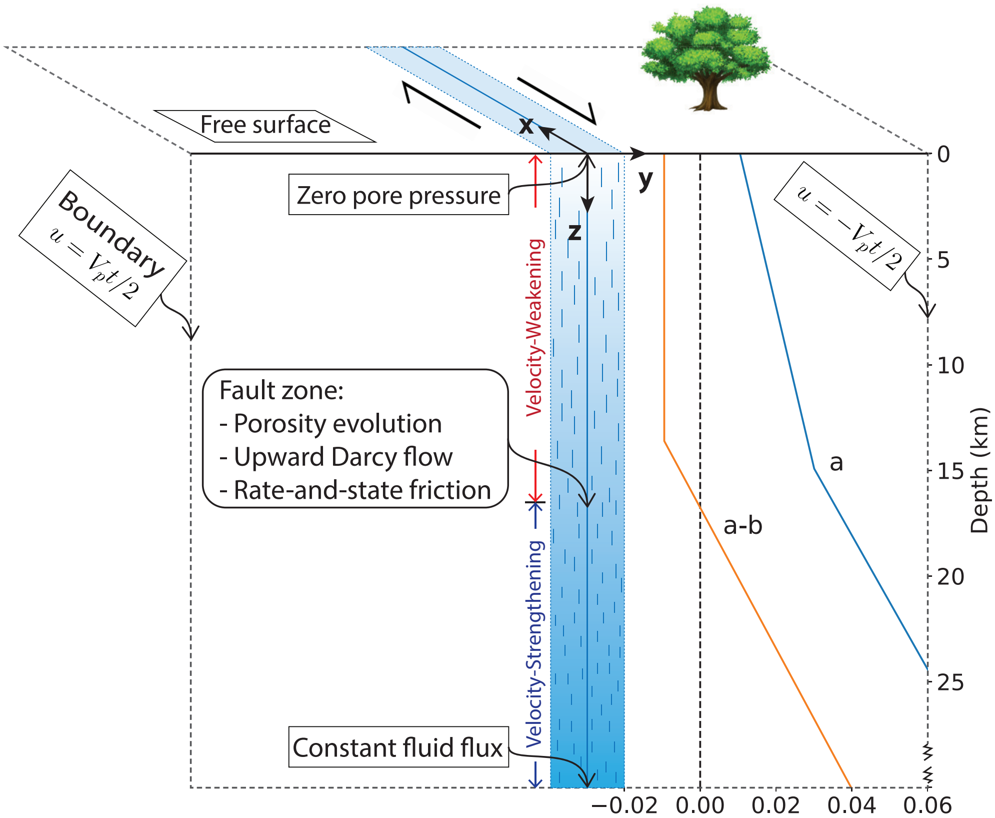

Figure 1. Strike-slip earthquake sequence simulations in a linear elastic solid with rate-and-state friction, fault zone fluid transport, and pore pressure evolution; distributions of rate-and-state parameters a and $a-b$ are shown on the right. Modified from Zhu et al. (2020).

For the computation of the rate-and-state friction coefficient, we use the regularized form (Rice et al., 2001):

$$f(\theta, V) = a \sinh^{-1}\left(\frac{V}{2V^*} e^{f^*/a} (\frac{V^*\theta}{d_c})^{b/a}\right), \tag{6}$$

where a is the direct effect parameter and V^* is the reference velocity. We use the aging law for state evolution (Ruina, 1983; Marone, 1998):

$$G(\theta, V) = \frac{bV^*}{d_c}(\frac{d_c}{V^*\theta} - \frac{V}{V^*}). \tag{7}$$

Apart from the fault boundary condition, the computational domain during the quasi-dynamic phase has three other boundary conditions:

$$\sigma_{xz}(y, 0, t) = 0, \quad \sigma_{xz}(y, L_z, t) = 0, \quad u(L_y, z, t) = \frac{V_L t}{2}, \tag{8}$$

where L_y and L_z are dimensions of the domain in the y and z directions. The boundaries perpendicular to the fault are traction-free, and the displacement condition on the remote boundary parallel to the fault provides steady loading consistent with slip velocity V_L. During the fully dynamic phase, we continue to enforce the friction law on the fault and free surface condition on the top boundary, but we switch at a nonreflecting condition on the side and bottom boundaries, consistent with the radiation condition that permits outgoing waves. We use a sufficiently large simulation domain to ensure that the solution is relatively insensitive to L_y and L_z, as explored by Erickson et al. (2022).

3.2 Porosity, Permeability and Fluid Equations

Fluid transport and pore pressure evolution are confined to a fault zone of constant width. As explained in the Introduction, the relevant transport properties of the fault zone should be regarded as those of the higher permeability and storage damage zone surrounding the slip surface.

We describe the evolution of fault zone porosity, ϕ, by additively decomposing it into elastic, viscous, and plastic components:

$$\dot{\phi} = \dot{\phi}_{\text{elastic}} + \dot{\phi}_{\text{viscous}} + \dot{\phi}_{\text{plastic}}, \tag{9}$$

where the overdot denotes a partial time derivative.

Elastic changes in porosity are governed by (Walder & Nur, 1984; Mavko et al., 2020)

$$\frac{\dot{\phi}_{\text{elastic}}}{\phi} = \beta_\phi \frac{\partial p}{\partial t}, \tag{10}$$

where β_ϕ is the elastic pore compressibility. This can be integrated, with fixed total stress, to obtain

$$\phi = \phi_0 e^{-\beta_\phi \sigma'}, \tag{11}$$

where ϕ_0 is the porosity at zero effective stress. While some experiments are better fit by adding a residual porosity (Rutqvist et al., 2002), that is, a nonzero value for ϕ in the large σ' limit, we neglect this complication in our study.

We model the viscous porosity change using a thermally activated linear creep law with compaction occurring in response to nonzero effective normal stress (Skarbek & Rempel, 2016; Yarushina et al., 2020):

$$\frac{\dot{\phi}_{\text{viscous}}}{\phi} = -\sigma' A e^{-E_a/RT} = -\frac{\sigma'}{\eta_s}, \tag{12}$$

where E_a is the activation energy, R is the ideal gas constant, T is the temperature, and A is a rate factor. We can interpret η_s/ϕ as an effective bulk viscosity of the porous rock that arises from deviatoric viscous strain in the matrix surrounding the pores, in which interpretation η_s is approximately the shear viscosity of the matrix. Similar equations describe compaction driven by pressure solution-deposition processes (Walder & Nur, 1984; Renard et al., 2000; Gratier et al., 2013). In either case, there is a strong dependence on temperature that appears here in a standard Arrhenius term. The interpretation of η_s as the matrix shear viscosity is most valid for equidimensional (spherical or ellipsoidal) pores, whereas for crack-like pores, the effective bulk viscosity is comparable to the matrix shear viscosity with minimal dependence on porosity (Sleep & Blanpied, 1992, 1994). Equation (12) shows that compaction occurs over time scale $t_c = \eta_s/\sigma'$.

In the absence of a porosity production mechanism, viscous creep closure of pores would occur until either all fluids are expelled from the pores or, in an undrained case, pressure equilibrates with the confining stress. There is no steady state solution with nonzero effective normal stress in this case, which is unreasonable for an active fault. Therefore we must account for slip-induced fracturing and other inelastic deformation processes that increase porosity. The specific processes in the seismogenic zone include cracking and fracturing in the fault damage zone during the passage of the stress concentration at the rupture front (McGrath & Davison, 1995; Kim et al., 2004) as well as dilatancy during sliding and shear of geometrically complex surfaces and structures (Lockner & Byerlee, 1994; Segall & Rice, 1995; Faulkner et al., 2010; Proctor et al., 2020; Brantut, 2020). Below the seismogenic zone, the processes that maintain porosity are less well understood, but may also involve brittle deformation and fracturing. Crack-seal shear and extension veins in subduction mélange provide evidence of frictional sliding and tensile fracturing at near-lithostatic fluid pressures (Ujiie et al., 2018; Schmidt & Platt, 2022; Condit & French, 2022), and hydraulic gradients established by local and cyclic pressure variations during viscous creep can drive episodic fluid escape and result in brittle-viscous fault slip (Menegon & Fagereng, 2021; Behr & Bürgmann, 2021). Much work is needed to formulate appropriate mathematical descriptions of these complex processes. Here we utilize an extension of the Segall and Rice (1995) plastic porosity evolution model for dilatancy:

$$\dot{\phi}_{\text{plastic}} = \frac{V}{L}(\phi_{\max} - \phi), \tag{13}$$

where L is the porosity enhancement length scale and

$$\phi_{\max} = \left(\phi_0 + \epsilon \ln \frac{V}{V_0}\right) e^{-\beta_\phi \sigma'} \tag{14}$$

is the steady state porosity. The steady state porosity increases with the logarithm of slip velocity V with a sensitivity quantified by the dilatancy coefficient ϵ. Experiments suggest values of ϵ on the order of 10^{-4} (Marone et al., 1990; Segall & Rice, 1995; Samuelson et al., 2009). We have added a dependence of $\phi_{\max}$ on the effective normal stress to account for the elastic dependence of porosity on effective stress. Furthermore, ϕ_0 itself is the maximum porosity reachable at zero effective stress at the slip velocity $V = V_0$. The porosity enhancement time scale is $t_e = L/V$.

We have chosen the porosity enhancement length scale as $L = 1$ m, which leads to comparable compaction and dilation time scales in the region below the seismogenic zone, which as we show develops a spatially uniform porosity distribution under steady state conditions. We recognize that in some studies L is chosen to be the same as d_c, the state evolution distance (Segall & Rice, 1995; Liu & Rubin, 2010), based on the assumption that dilatancy occurs within the shearing gouge layer or nonplanar slip surface. In contrast, our model, focusing on longer timescales, is concerned with dilatancy occurring within the much broader damage zone through which along-fault fluid transport occurs. Another conceptual model, which may be relevant below the seismogenic zone, is of a distributed ductile shear zone (Sibson, 1983; Hughes et al., 2020; Cawood & Platt, 2021). In this latter case, the ratio L/w, w being the shear zone width, can be interpreted as the critical strain for porosity evolution. The discussion above suggests that L might best be chosen as a depth-dependent quantity, selected based on the nature of localized or distributed deformation and the width of the shear zone. However, to simplify the model setup, we have chosen L to be independent of depth.

Combining the expressions above, we write the elastic, viscous, and plastic evolution of porosity as

$$\frac{\partial \phi}{\partial t} = \phi \beta_\phi \frac{\partial p}{\partial t} - \frac{\phi \sigma'}{\eta_s} + \frac{V}{L}(\phi_{\max} - \phi). \tag{15}$$

Conservation of fluid mass, together with a linearized fluid equation of state, Darcy's law in a uniform-width fault zone, and the porosity evolution equation, leads to the 1D pressure diffusion equation:

$$\phi\beta \frac{\partial p}{\partial t} = \frac{\partial}{\partial z}\left(\frac{k}{\eta_f}\frac{\partial p}{\partial z}\right) - \dot{\phi}_{\text{viscous}} - \dot{\phi}_{\text{plastic}} \tag{16}$$

$$= \frac{\partial}{\partial z}\left(\frac{k}{\eta_f}\frac{\partial p}{\partial z}\right) + \frac{\phi \sigma'}{\eta_s} - \frac{V}{L}(\phi_{\max} - \phi) \tag{17}$$

where $\beta = \beta_f + \beta_\phi$ is the sum of the fluid and pore compressibility, η_f is the fluid viscosity, and $k = k(\phi)$ is the porosity-dependent permeability. The absence of the $\rho_f g$

term reflects the fact that we have defined p as the overpressure, i.e., pressure in excess of hydrostatic pressure. Viscous and plastic porosity evolution manifest as source terms in the pressure diffusion equation. The fluid flux, expressed as the Darcy velocity, is given by

$$q = \frac{k}{\eta_f}\frac{\partial p}{\partial z}. \tag{18}$$

The absence of a minus sign means that q is positive for upward flow (in the $-z$ direction).

Next we introduce a model for permeability. In this study we assume a power-law relation between porosity and permeability, which has been widely documented experimentally (Walder & Nur, 1984; Nelson, 1994; Zhu et al., 1995; Civan, 2001; Im et al., 2018):

$$\frac{k}{k_0} = \left(\frac{\phi}{\phi_0}\right)^{\alpha}, \tag{19}$$

where k_0 and ϕ_0 are the reference permeability and porosity and α is an exponent. Although the exponent α can have a wide range of values depending on the rock type and underlying processes which change the pore space, we have chosen $\alpha = 3$ here due to its common usage in the literature (Schulz et al., 2019). Equation (19) is consistent with the experimentally observed dependence of permeability on effective stress, which is commonly expressed as $k = k_0 e^{-\sigma'/\sigma^*}$, where σ^* is a stress sensitivity parameter (Rice, 1992). This expression follows directly from the elastic dependence of porosity on effective stress given by Equation (10) and the porosity-permeability relation (19), which combine to give $k = k_0 e^{-\alpha\beta_\phi\sigma'}$. The stress sensitivity parameter is identified as $\sigma^* = (\alpha\beta_\phi)^{-1}$.

In our model, we keep k_0 constant. However, there is also an option to evolve k_0 to account for the evolution of tortuosity and pore connectivity (Matyka et al., 2008; Ghanbarian et al., 2013). Even when porosity changes are negligible, the permeability could still be enhanced by slip and deformation if the connectivity of the pore space is greatly improved, especially in low porosity rocks. This possibility was explored by Zhu et al. (2020), who accounted only for elastic changes in ϕ and focused on permeability evolution and fault valving from evolution of k_0 rather than ϕ. Here we take the opposite approach and account for changes in k only in response to changes in ϕ with k_0 held fixed.

The pressure diffusion equation (17) requires two boundary conditions. At the free surface, we hold pressure fixed at its hydrostatic value: $p(0,t) = 0$. At the base of the model, we assume a constant fluid source: $q(L_z, t) = q_0$. This relegates fluid sources to depths well below the seismogenic zone. An important extension of our model is to account for fluid sources within the seismogenic zone and beneath it where slow earthquakes occur.

3.3 Numerical Method

We use a high-order SBP-SAT finite difference method for spatial discretization along with adaptive Runge-Kutta time stepping, with error control on slip and the state variable (Erickson & Dunham, 2014; Allison & Dunham, 2018; Duru et al., 2019). Pressure (17) and elastic porosity (10) are solved implicitly using backward Euler (using operator-splitting at the Runge-Kutta stage level), while slip (2), state variable (7), viscous and plastic porosity (12,13) are solved explicitly with the adaptive Runge-Kutta method (Zhu et al., 2020; Yang & Dunham, 2021).

The spatial discretization along the fault is chosen to adequately resolve the nucleation length for the aging law based on Equation (42) in Rubin and Ampuero (2005):

$$L_\infty \approx \frac{1}{\pi}\left(\frac{b}{b-a}\right)^2 L_b, \tag{20}$$

where $L_b = \mu D_c / b\sigma'$ (Dieterich, 1992). We use the value of σ' from the initial steady-state solution for this computation. Then we take the minimum value of L_∞ and resolve it using 20 grid points for the velocity-weakening part of the fault. We apply grid stretching starting from the velocity weakening to velocity strengthening transition all the way down to the bottom of the domain. Grid stretching is also applied in the fault-normal direction, with dense grids near the fault, and sparser grids away from the fault.

4 Steady-State Solution Balancing Viscous Creep Closure and Dilatancy

In this section, we develop and examine the steady state solution to the governing equations. This solution provides insight into the nominal distribution of porosity, permeability, pressure, and effective normal stress with depth. We also utilize this solution as the initial condition for time-dependent earthquake sequence simulations, wherein the solution departs rapidly from steady state to produce earthquakes and slow slip. This demonstrates that the steady state solution is unstable to perturbations. Whether the instability arises from velocity-weakening friction, fluid coupling, or some combination thereof should be assessed through linear stability analysis, which is beyond the scope of this study.

To find the steady state solution, we set $\partial p/\partial t = 0$, $\partial \phi/\partial t = 0$ and $V = V_0$ equal to the plate loading rate. Balancing viscous compaction (12) with dilatancy (13) provides an expression for porosity in terms of effective normal stress:

$$\phi = \frac{\phi_0 e^{-\beta_\phi \sigma'}}{1 + t_e/t_c}. \tag{21}$$

We also have Darcy's law (18), which at steady state (with flux equal to the specified influx q_0) reads

$$\frac{dp}{dz} = \frac{\eta_f q_0}{k}, \tag{22}$$

where the porosity-dependent permeability k is evaluated using (21) in (19). Substituting this expression into (22) and using $\sigma' = \sigma_0' - p$ yields a first order nonlinear differential equation for the steady state $p(z)$ that can be integrated downward in z with initial condition $p(0) = 0$.

The set of parameters shown in Table 1 is used in the steady-state calculation and earthquake sequence simulations. We select a 30 K/km geotherm for consistency with previous modeling (Allison & Dunham, 2018). The fault total normal stress minus the hydrostatic pore pressure is assumed to increase linearly as $d\sigma_0'/dz = 12.2572$ MPa/km, based on Equation (14) in Allison and Dunham (2018). Fluid transport properties exhibit considerable variation and there are limited constraints on properties at the depths of interest to us. We select an elastic pore compressibility of $\beta_\phi = 10^{-8}$ Pa^{-1} based on studies of the tidal response of water levels in wells near the San Andreas and other faults (Xue et al., 2013, 2016; Guo et al., 2021). The reference porosity $\phi_0 = 0.1$ and permeability $k_0 = 2 \times 10^{-16}$ m^2 are selected to provide a steady state permeability profile comparable to Zhu et al. (2020). A steady fluid source with influx of $q_0 = 10^{-9}$ m/s is imposed at the bottom of the fault, which is within the range of fluxes inferred for continental plate boundary faults (Kennedy et al., 1997; Menzies et al., 2016).

The solution we obtain for steady-state overpressure, effective normal stress, porosity, permeability, and the compaction/enhancement times is shown in Figure 2. We compare solutions for three values of the rate factor A: $A = 5{\times}10^{-14}$ Pa^{-1} s^{-1} (solid line), which is selected as the reference case, and two comparison cases, $A = 5{\times}10^{-15}$ Pa^{-1} s^{-1} (dotted line) and $A = 5 \times 10^{-13}$ Pa^{-1} s^{-1} (dashed line). Increasing A is similar to increasing the geothermal gradient or decreasing the activation energy. For the upper 2–3 km, the pore pressure is approximately hydrostatic and the effective stress σ'

Symbol	Description	Value
L_z	Domain size in z direction	100 km
L_y	Domain size in y direction	100 km
T_0	Surface temperature	293 K
T	Temperature	30 K/km geotherm
E_a	Pressure solution activation energy	40 kJ mol^{-1}
R	Ideal gas constant	8.32 J mol^{-1} K^{-1}
A	Flow law prefactor	5×10^{-14} Pa^{-1} s^{-1}
η_f	Fluid viscosity	10^{-4} Pa s
β_f	Fluid compressibility	10^{-9} Pa^{-1}
β_ϕ	Elastic pore compressibility	10^{-8} Pa^{-1}
ϕ_0	Porosity at zero stress	0.1
ϵ	Dilatancy coefficient	2×10^{-4}
L	Porosity enhancement length scale	1 m
k_0	Permeability at ϕ_0	2×10^{-16} m^2
α	Exponent for porosity-permeability relation	3
q_0	Fluid injection rate from the bottom	10^{-9} m/s
V_0	Initial slip velocity	10^{-9} m/s
V^*	Reference slip velocity	10^{-6} m/s
f^*	Reference friction coefficient at V^*	0.6
d_c	State evolution distance	2 mm

Table 1. Parameters used for steady-state calculation and earthquake sequence simulations.

increases linearly. The porosity and permeability are also relatively high in this region, but they experience a rapid decrease as σ' increases due to the elastic porosity response to effective normal stress. At about 5–10 km, σ' reaches a peak of about 90, 70, and 50 MPa, respectively, for increasing values of A. At this peak, porosity also reaches a minimum value as it decreases with increasing σ'. The effective stress σ' then starts to decrease due to compaction. The effect can be seen from Figure 2(d), which shows the time scales for compaction in red and dilatancy in blue. For higher values of A, the point at which dilatancy and compaction exactly balance each other is shallower and the compaction time is shorter. In all, the larger the value of A, the faster compaction happens especially at shallower depths, which results in higher overpressure, lower effective normal stress, and lower porosity and permeability.

Porosity and permeability approach constant values at sufficiently great depths. This asymptotic behavior as $z \to \infty$ can be understood as follows. We substitute (19) and (21) into (22), and then approximate $e^{-\beta_\phi \sigma'} \approx 1$ because effective stress is very low at depth, to obtain

$$\frac{dp}{dz} \approx \frac{\eta_f q_0}{k_0} \left(1 + \frac{t_e}{t_c}\right)^3 . \tag{23}$$

Next, we make the ansatz, to be verified below, that σ' approaches a constant value as $z \to \infty$ such that $d\sigma'/dz = d\sigma_0'/dz - dp/dz \to 0$. This allows us to replace dp/dz with the constant $d\sigma_0'/dz$ in (23), which we solve for the asymptotic behavior of the porosity enhancement to compaction time scale ratio:

$$\frac{t_e}{t_c} \approx \left(\frac{d\sigma_0'}{dz} \frac{k_0}{\eta_f q_0}\right)^{1/3} - 1. \tag{24}$$

Substituting parameter values into this expression, we obtain $t_e/t_c \approx 1.91$. Because $t_e = L/V_0 = 31.69$ yr is constant, this means $t_c = (Ae^{-E_a/RT}\sigma')^{-1} \approx t_e/1.91 =$

16.63 yr is also a constant, regardless of the compaction rate factor A. This explains why the compaction time approaches the same value at depth for all A in Figure 2. It also follows that porosity and permeability approach constant values, independent of A, specifically $\phi \approx \phi_0/(1+t_e/t_c) = 0.034$ and $k \approx k_0/(1+t_e/t_c)^3 = 8.16\times10^{-18}$ m^2. The limiting value of effective normal stress (which does depend on A) follows from the above expressions:

$$\sigma' \approx \frac{V_0}{LAe^{-E_a/RT}} \left[\left(\frac{d\sigma_0'}{dz} \frac{k_0}{\eta_f q_0} \right)^{1/3} - 1 \right]. \tag{25}$$

The original ansatz of constant σ' as $z \to \infty$ is justified.

We remark that the steady-state effective stress profile in Figure 2(a) differs from other models in the literature involving upward flow along faults, in particular the Rice (1992) model that includes the elastic dependence of permeability on effective stress. This model was also adopted by Zhu et al. (2020) for their steady state. The Rice (1992) model features pore pressure than transitions from the hydrostatic gradient near the surface to the fault normal stress gradient at depth, such that effective normal stress is constant over much of the seismogenic zone. This distribution of effective stress has been widely used in earthquake sequence modeling, following Rice (1993). Our model produces a similar distribution of effective stress near the surface and in the upper seismogenic zone, with overpressure developing in response to the elastic dependence of permeability on effective stress. However, after reaching a maximum within the seismogenic zone, it decreases toward a much lower value at depth due to the onset of compaction, which was neglected by Rice (1992).

5 Earthquake Sequence Simulations

Next we turn to earthquake sequence simulations. We start the simulations from steady-state conditions. The hydraulic steady state is described in the previous section. In addition, slip velocity is set to V_0 and state and friction coefficient to their steady state values. However, the steady state solution is unstable, and complex sequences of earthquakes and aseismic slip quickly emerge. We run our simulation for five earthquake cycles to spin up the system.

5.1 Reference Case

In this section, we examine the reference case with $A = 5\times10^{-14}$ Pa^{-1} s^{-1}. Figure 3(a) shows the space-time plot of slip velocity. We observe ruptures of the full seismogenic zone happening every 20-30 years, and between those large ruptures, there are about 2 partial ruptures at the base of the seismogenic zone. Leading up to each full or partial rupture is a set of SSEs that happen below the ascending locking depth, which advances about 4–5 km over the cycle. Figure 3(b) is a space-time plot of the effective normal stress over the same time period. Note that the effective stress departs from the steady state prediction, increasing during each earthquake as pore pressure decreases from dilatancy. In Figure 4 , we zoom into an 8-year period from about 50–58 years into the simulation (shown as a black box in Figure 3) to study the slow slip pattern in greater detail. In this region, where SSEs occur, the effective stress is between 30–40 MPa, much higher than in other models for slow slip. We return to this point in the Discussion.

Figure 4 shows spontaneously generated SSEs which occur about every year at the base of the seismogenic zone over a period of ∼8 years, gradually unlocking the fault and pushing the creep front upward before an earthquake occurs. Above the locking depth, the fault is below steady state (except during earthquakes), whereas below it, it is close to steady state, on average. We speculate that SSEs occur here because that steady state is unstable due to velocity weakening friction and compaction-driven pressurization. These SSEs have a wide range of behaviors. Some can last from a few months to a year, which

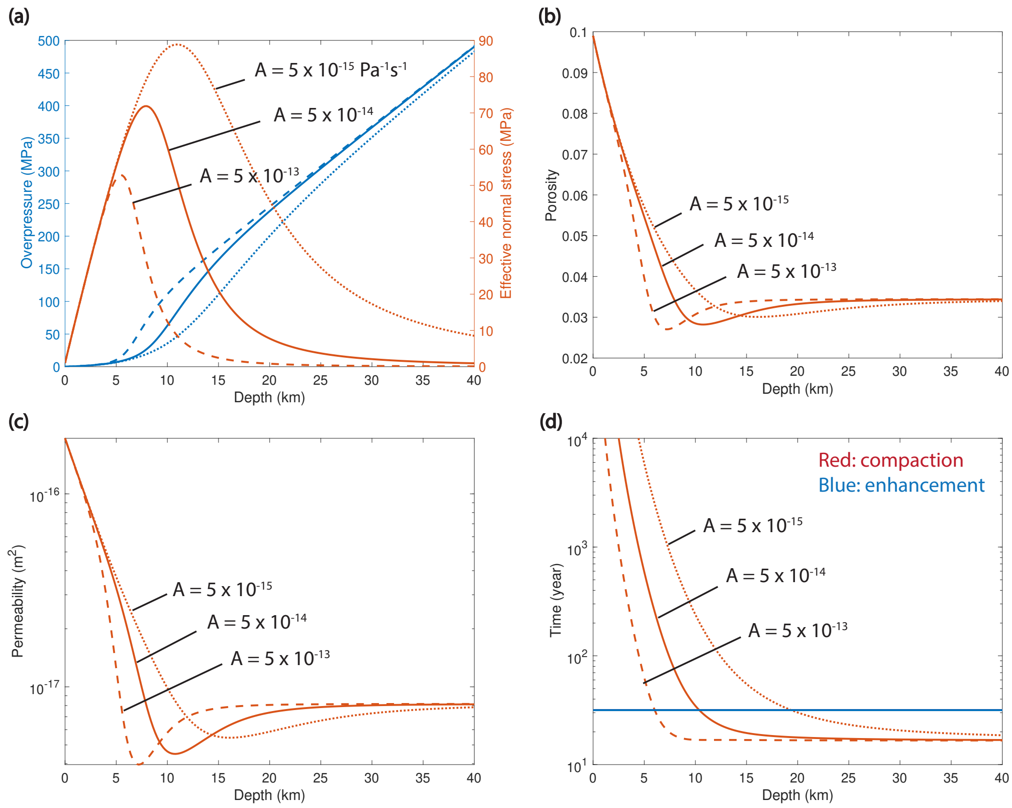

Figure 2. Steady-state solution for different values of compaction rate factor: $A = 5 \times 10^{-15}$ Pa^{-1} s^{-1} (dotted line), $A = 5 \times 10^{-14}$ Pa^{-1} s^{-1} (solid line), and $A = 5 \times 10^{-13}$ Pa^{-1} s^{-1} (dashed line). (a) Overpressure (blue) and effective normal stress (red), (b) porosity, (c) permeability, (d) porosity compaction time t_c (red) and enhancement time t_e (blue). The solution is shown to 40 km depth, but the steady state solution is solved for the entire 100 km domain.

are characteristic of long-term SSEs observed at some subduction zones, such as in south-west Japan in the Nankai subduction zone (Hirose & Obara, 2005; Matsuzawa et al., 2010; Kobayashi, 2017) and in New Zealand (Wallace et al., 2012; Wallace, 2020). There are also shorter-term, high-velocity SSEs that only last for a few days, marked by the deeper red colors that indicate their high velocity in Figure 4(b). We will zoom into these events in more detail later.

Overall, the SSEs are located between about 10–14 km depth, where the fault is entirely velocity weakening. The reason why SSEs nucleate in this region but not further down-dip can be seen in Figure 4(f), which shows the depth dependence of nucleation length. We calculate the nucleation length according to Equation (20) using σ' at the beginning of this period. It is likely that dilatancy, compaction, and fluid coupling alter the nucleation process and nucleation length, but we currently lack an alternative expression for nucleation length that accounts for these processes. Between 10–14 km, the nucleation length ranges from about 100 to 300 m, but below 14 km it grows rapidly to more than 1000 m. Complex SSE patterns occur in the region with short nucleation lengths, but where the nucleation length is larger we do not observe any instabilities.

The SSEs arise because of the velocity weakening friction instability, accelerated in timing by compaction-induced pressurization, but with the increase in slip velocity stalled by dilatancy. The pressure and porosity change relative to the beginning of the

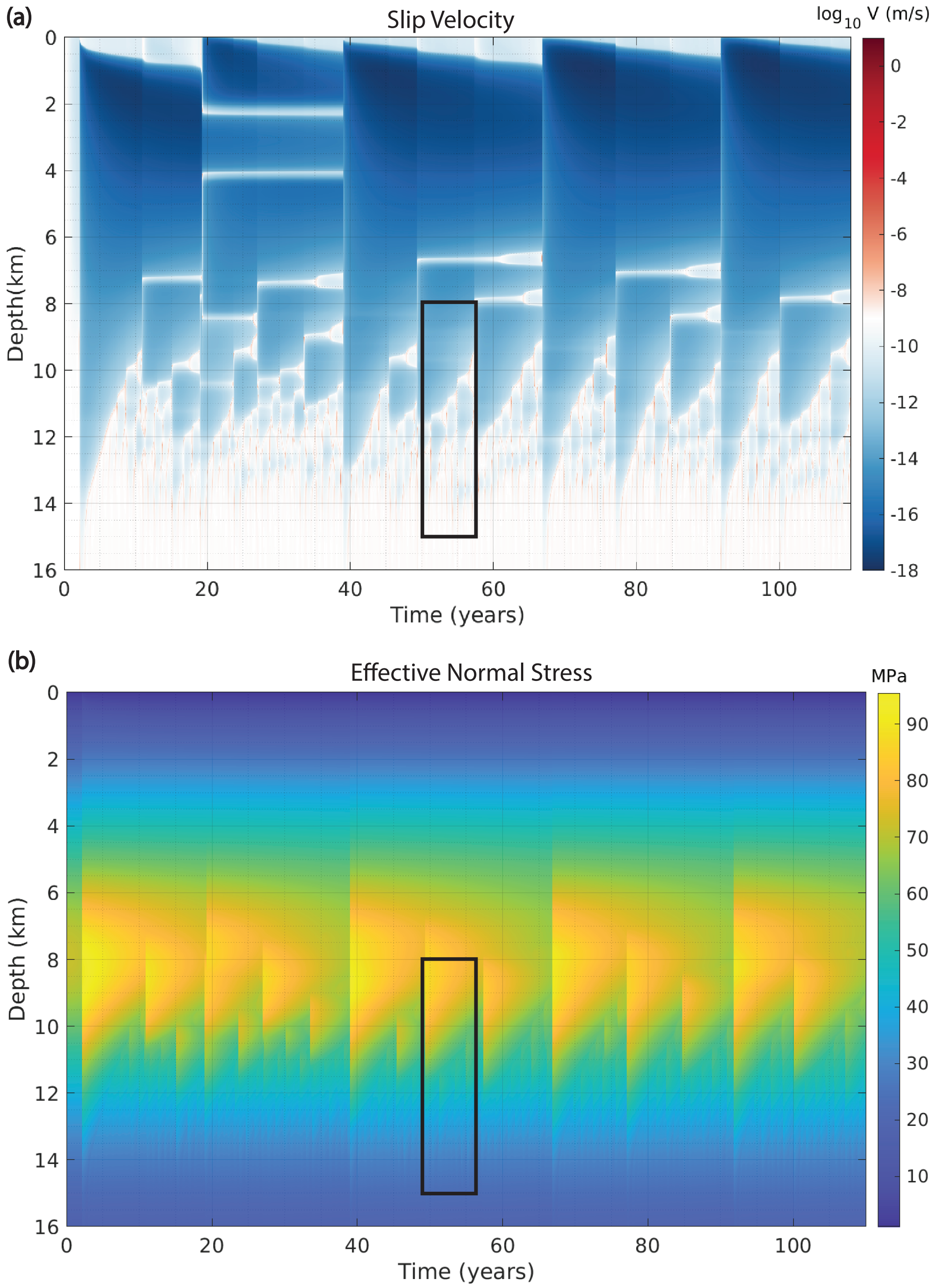

Figure 3. Space-time plot of (a) slip velocity and (b) effective normal stress over 110 years of simulation time. The entire region shown is velocity weakening.

selected time period are shown in Figure 4(c) and (d). Before each SSE occurs, compaction-driven pressurization weakens the fault and causes it to slip. When slip happens, dilatancy opens pore space, reduces pressure and strengthens the fault, limiting slip velocity. The occurrence of slip reduces shear stress and slip velocity eventually decelerates. Compaction again dominates dilatancy and causes the pressure to rise, and in this fashion the chain of SSEs is generated. Each successive SSE is able to propagate further into the shallower section of the fault due to elastic stress transfer during the unlocking process. Moreover, pressurization of the fault above the locking depth, which is creeping at velocities below the plate rate, is driven by pore compaction. Consider the fault at 9.5 km depth, which at the end of the SSEs has experienced a nearly 20 MPa pore pressure increase. Dilatancy can be ignored here since the slip velocity in this time window is much lower than the plate loading rate. The compaction time scale at this depth is $t_c \approx 1200$ years, so that the pressurization rate from compaction is $(t_c\phi\beta)^{-1} \approx 2.5$ MPa/yr. For a period of about 8 years before the earthquake occurs, the pressure increase is approximately 20 MPa. Finally, when a stress concentration has been built up in the lower seismogenic zone where the fault is sufficiently weakened by pressurization, an earthquake nucleates, resets the shear stress level, and the cycle continues in another episode.

We also note that due to the small porosity changes as shown in Figure 4(d), the permeability changes accompanying these SSEs are also very minor. This means that changes in fluid flux, shown in Figure 4(e), are concentrated immediately behind advancing slip fronts where pressure gradients are largest as a consequence of dilatant suctions. Fluids flow from the undilated region ahead of the slip front into the dilated region behind it, and this flow can be either upward (for a slip front advancing downward) or downward (for a slip front advancing upward). Elevated fluxes and reversals in flow direction are confined to regions extending no more than a few hundred meters and persist only for days to months, after which flow returns to its steady state value. This stands in contrast to the SSEs that are driven by fault valving and upward fluid migration as seen in Zhu et al. (2020), where flow is always upward and flux varies over four orders of magnitude. We return to this comparison in the Discussion.

We now take a closer look at the SSE that happens about 2 years into the time window shown in Figure 4(a). This event is rather characteristic of the complex behavior of slow slip in the simulation. The zoomed-in view of the slip velocity is shown in Figure 5(a), which spans 3 years. During this time, we first have a spontaneously generated slow slip transient starting at around 2.5 years from a depth of approximately 14 km that propagates upward. When it reaches 13 km depth after about 2–3 months, the slip front splits into an upward- and a downward-propagating front. The downward front slows down and stabilizes, whereas the upward front continues unlocking the fault and eventually merges with another crack tip, which nucleates at 11.5 km depth about 3 years into the time window. Moreover, at 3.5 years and 4.3 years, close to 13 km depth, two more such events nucleate, propagating both up and down. Figure 5(b), which shows the pressure change, illustrates the interaction between compaction and dilatancy. Dilatancy creates suctions of a few MPa during each event, while compaction in regions of the fault below steady state continues to pressurize and weaken the fault.

The interaction among slip velocity, porosity, and pressure during the 2–5-year period can be more clearly seen in Figure 6, where we plot porosity change, pressure change, and slip velocity at 11.5 km depth for the same time interval shown in Figure 5 (with changes in porosity and pressure calculated with respect to those values at time zero in Figure 4). At first, pressure starts to increase as the pores compact. Slip velocity remains low until the passage of an SSE between time steps 660–680 (or around 3.2 years) that increases slip velocity to about 10^{-8} m/s. When slip occurs, dilatancy causes a pressure drop that strengthens the fault. This strengthening contributes to the arrest of the SSE and brings the slip velocity down to the loading rate.

We can understand the quantitative controls on porosity change, and hence permeability, during rapid slip (earthquakes and SSEs) as follows. Rapid slip means that pressure changes from compaction and fluid flow can be neglected, and we write Equa-

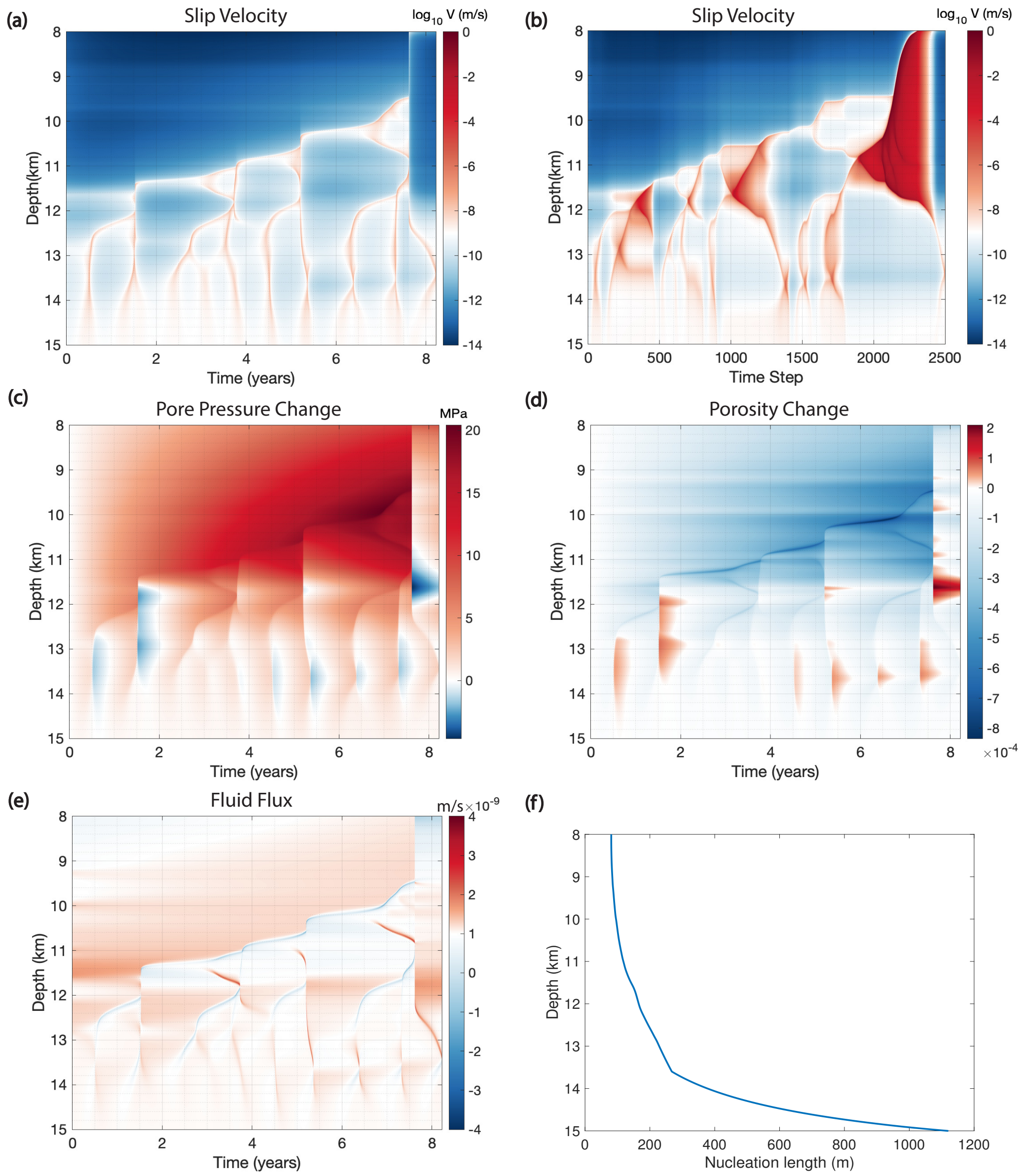

Figure 4. Results from about 50 years into the reference simulation, plotted for depth range 8–15 km over about 8 years, illustrating representative SSE behavior in our simulations. Space-time plots of (a) $\log_{10}$ slip velocity with time on the x-axis, (b) $\log_{10}$ slip velocity with simulation steps on the x-axis, (c) pressure change, (d) porosity change from the beginning of this period, and (e) fluid flux. (f) Nucleation length variation with depth, evaluated using the effective normal stress distribution at the beginning of this period.

tions (15) and (17) as

$$\dot{\phi} \approx \phi\beta_\phi\dot{p} + \dot{\phi}_{\text{plastic}}, \tag{26}$$

and

$$\phi\beta\dot{p} \approx -\dot{\phi}_{\text{plastic}}, \tag{27}$$

which combine to yield

$$\dot{\phi} \approx \left(1 - \frac{\beta_\phi}{\beta}\right) \dot{\phi}_{\text{plastic}} = \frac{\beta_f}{\beta_f + \beta_\phi} \dot{\phi}_{\text{plastic}}. \tag{28}$$

Therefore, the larger the pore compressibility β_ϕ is compared to the fluid compressibility β_f (and thus the closer β_ϕ/β is to unity), the smaller the change in total porosity when the fault slips. Note that small changes in porosity do not preclude substantial pressure changes from dilatancy, which are dictated by changes in plastic porosity rather than total porosity. The importance of β_ϕ/β was recognized in a similar manner by Dal Zilio, Hegyi, et al. (2022).

After the first SSE arrests around time step 700, the slip front of the SSE that was generated deeper propagates upward and merges with the SSE that nucleated at 11.5 km. The merging of these slip fronts causes a faster SSE to nucleate at about 11.8 km, which continues to drive the slip front upwards and raise the locking depth. This shows up as the second velocity peak in Figure 6, reaching between 10^{-7}–10^{-6} m/s. Dilatancy produces a larger pressure drop here than for the previous slower event. After this slip front passes and slip velocity drops below the loading rate, compaction again becomes the dominant process and pressurizes the fault. Although all SSEs could be considered as failed nucleations of an earthquake, some reach higher slip velocities in response to the build-up of spatially average shear stress from deeper slip, or due to stress concentrations left behind by previous ruptures.

The amount of slip at 11.5, 12.5, and 13.5 km depth is plotted in Figure 5(c). At 12.5 and 13.5 km depth, slip accumulates in a more continuous manner, with fastest increases of 1–2 cm of slip during the passage of each slip front that spans a few months. At 11.5 km, a sharp increase in slip between 3.5 and 4 years is attributed to the rapid SSE caused by the merging of an upward- and a downward- propagating slip front. This event creates about 3 cm of slip over only a few days. The shear strength of the fault at the same locations is plotted in Figure 5(d). Strength drops during the passage of the SSEs can exceed 1 MPa but stress drops are generally much smaller. Thus, there is a diversity of slip behavior including both long-term events and high-velocity short-term events. Both can propagate upward and downward, accumulating varying amounts of slip and experiencing different stress and strength drops.

5.2 Comparison with Different Compaction Rate Factors A

In this section, we compare earthquake sequence simulation results for different values of the compaction rate factor A, as examined earlier in the context of the steady state solution (Figure 2). Changing A alters the compaction time scale and hence the depth at which compaction time becomes shorter than the porosity enhancement time scale. As we show, this is the primary control on the depth of SSEs. Observe from the space-time plots of slip velocity in Figure 7 that for the higher value of $A = 5 \times 10^{-13}$ Pa^{-1} s^{-1}, the recurrence time interval of large earthquakes has been reduced to less than 10 years, and the location of the SSEs shallows to about 5–9 km depth. This is because higher A causes faster compaction-driven pressurization and weakening. Figure 7(c) shows a zoomed-in view of the boxed region in Figure 7(a). SSEs are spontaneously generated above 9 km depth. The earlier events have a single slip front that propagates upward, but the same type of complexity seen for the reference case emerges for later events at shallow depths of 6–7 km. Here, nucleation drives SSEs both upward and downward, and SSEs merge to nucleate subsequent events with faster slip velocities and shorter durations. A short nucleation length on the order of 100–300 m, as shown in Figure 7 (e), is again responsible for the complex SSEs.

On the other hand, when the compaction rate factor is decreased by an order of magnitude from its reference value to $A = 5 \times 10^{-15}$ Pa^{-1} s^{-1}, the recurrence inter-

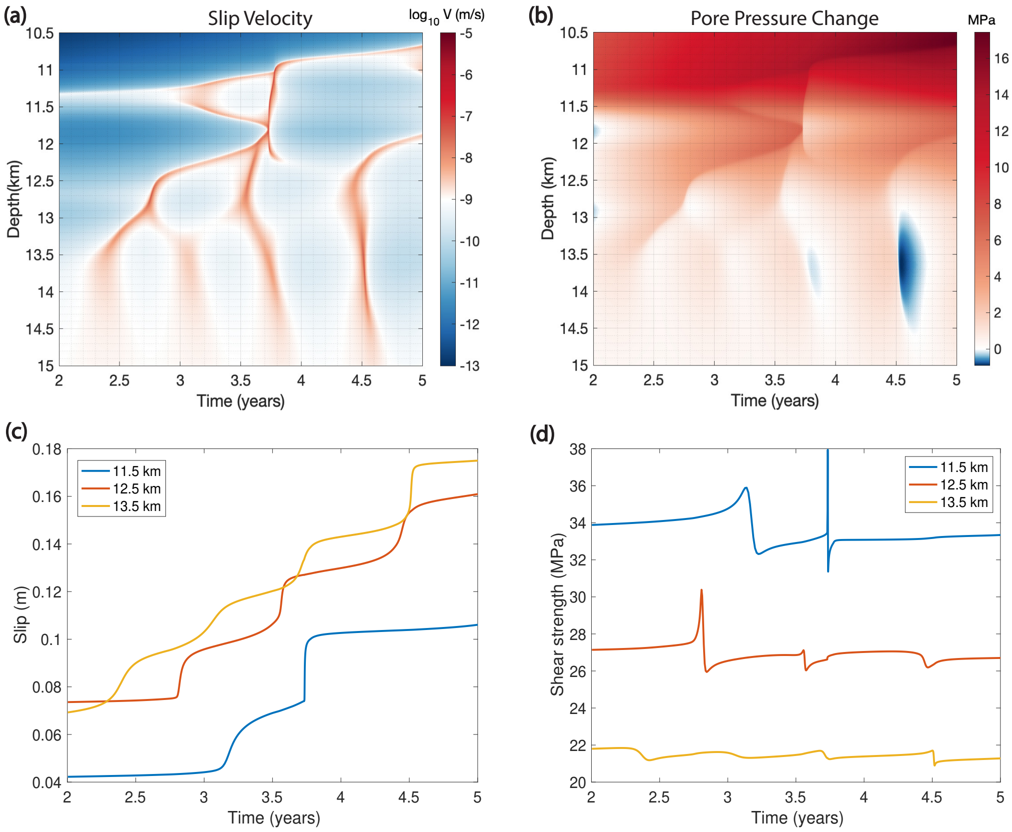

Figure 5. Zoomed-in space-time plot of (a) slip velocity and (b) pressure change (relative to the beginning of the period in Figure 4) of several SSEs. (c) Accumulated slip and (d) fault shear strength at 11.5, 12.5, and 13.5 km depth.

val of large earthquakes increases to about 50 years. The location of SSEs moves deeper to about 14–18 km, where the fault transitions from velocity weakening to velocity strengthening. In Figure 7 (d), we do not see the same complex slip patterns as before, since the region hosting SSEs has longer nucleation lengths due to $a-b$ becoming closer to zero. However, SSEs still spontaneously nucleate below the locking depth and propagate primarily upward, each pushing the locking depth upward by several hundred meters.

For all three compaction rate factors A, SSEs occur in regions where the compaction time becomes comparable to the porosity enhancement time, as shown in Figure 2(d). For $A = 5 \times 10^{-13}$ Pa^{-1} s^{-1}, the two time scales are equal at around 6 km, for $A = 5 \times 10^{-14}$ Pa^{-1} s^{-1}, at 10 km, and for $A = 5 \times 10^{-15}$ Pa^{-1} s^{-1}, at 19 km. For the first two cases, SSEs occur slightly below the depth at which the two time scales are equal, as the fault needs to pressurize and weaken to trigger nucleation of the SSEs, so compaction should dominate over dilatancy at steady sliding conditions. For the last case, SSEs occur above the point of equality, since at 19 km, the fault has already transitioned from velocity weakening to velocity strengthening friction, where it only undergoes stable sliding. This suggests that velocity weakening friction might be a necessary condition for the nucleation and propagation of SSEs in our model. However, the strong influence of the compaction rate factor demonstrates that compaction-driven pressurization and weakening is of fundamental importance for generating SSEs and we cannot rule out the possibility that compaction might permit unstable slip for velocity strengthening friction.

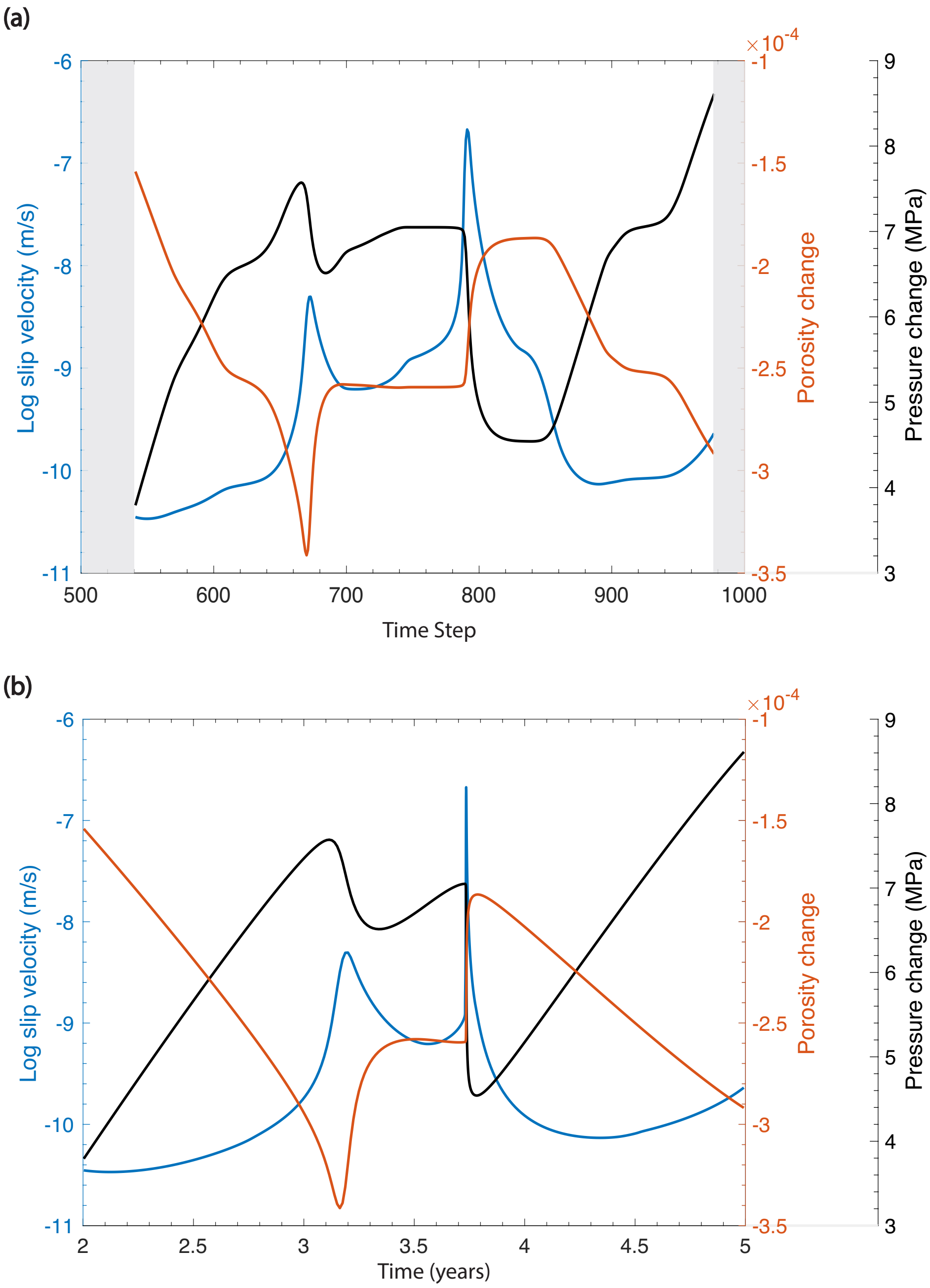

Figure 6. Time series of different fields plotted at 11.5 km depth for the time period in Figure 5: $\log_{10}$ slip velocity (blue), porosity change (red), and pressure change (black) from the beginning of the period in Figure 4. (a) is shown in time steps, (b) is shown in years.

6 Discussion

In this study we have explored the role of thermally activated compaction-driven pressurization in controlling the occurrence of earthquakes and slow slip events. The slip produced by the SSEs in our simulations is on the order of centimeters, spanning a few days to a few years, making them geodetically detectable using GNSS stations and InSAR (Klein et al., 2018; Jolivet & Frank, 2020). The duration and amount of slip of the

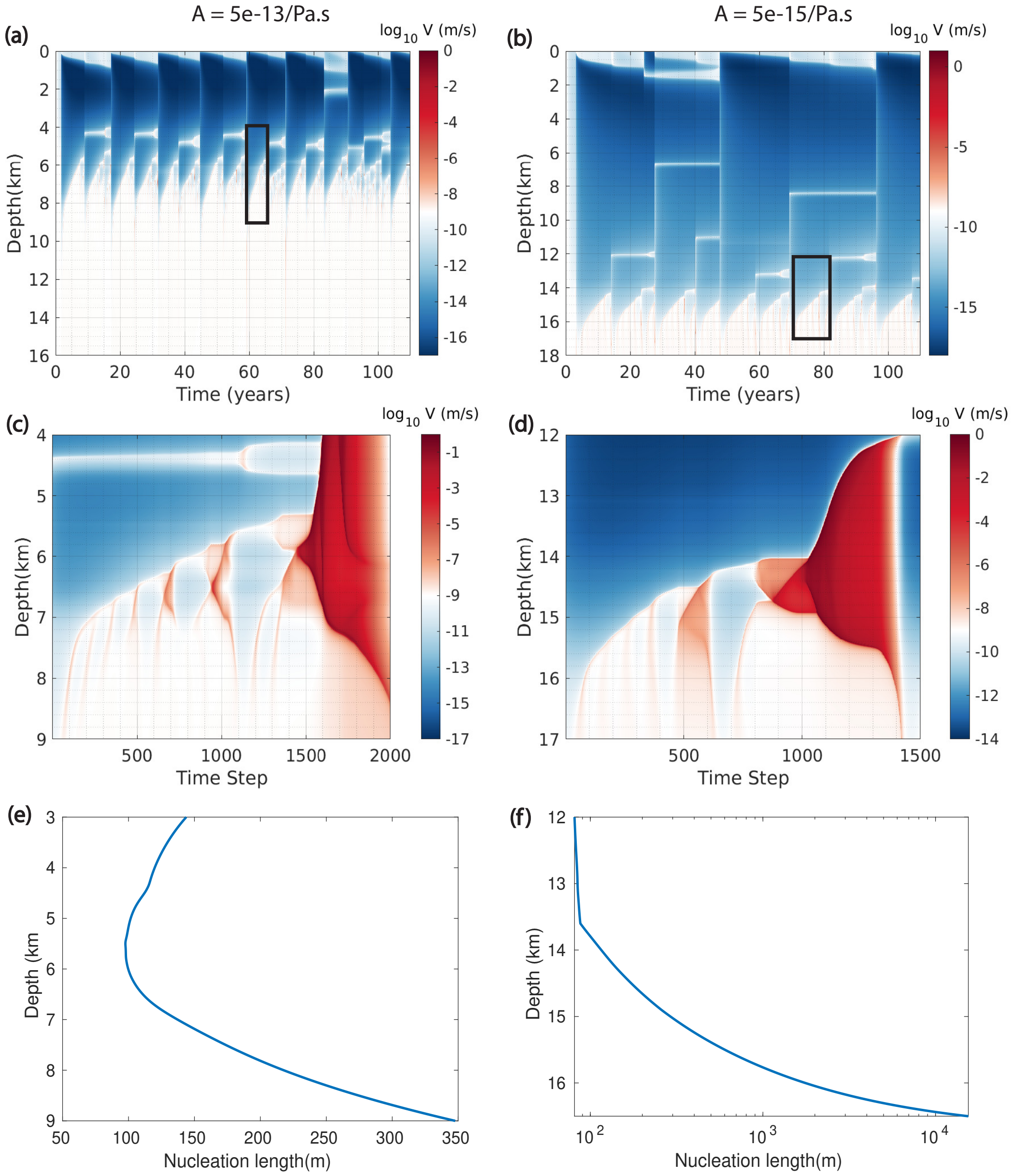

Figure 7. Left column: $A = 5 \times 10^{-13}$ Pa^{-1} s^{-1}. Right column: $A = 5 \times 10^{-15}$ Pa^{-1} s^{-1}. (a), (b): Space-time plots of slip velocity over 110 years. (c), (d): Zoomed-in slip velocity in the region in black box from (a) and (b), note x-axis is time steps of the selected time window. (e), (f) Depth-dependent nucleation length, note in (f), the x-axis is in log scale, since the fault is transitioning from velocity weakening to velocity strengthening starting from about 14 km, $a - b$ becomes closer to zero (velocity neutral) at greater depths, causing the nucleation length to increase by a few orders of magnitude.

SSEs are also in accordance with observations in many subduction zones (Peng & Gomberg, 2010; Radiguet et al., 2011; Araki et al., 2017; Wallace, 2020). However, we note that our model is but one of many models that reproduce geophysically observable constraints on SSEs. This highlights the importance of falsifying models based on geologic and experimental constraints on fault zone structure and the processes controlling pore pressure dynamics and the evolution of fault strength.

Our model can be viewed as an end-member case in which permeability is controlled exclusively by porosity, which evolves in response to creep compaction and dilatancy as well as elastic pore compressibility. In our simulations, the changes in porosity and therefore permeability are quite small. This is because dilatancy-driven porosity increase from slip is approximately balanced by elastic porosity reduction from the pressure drop. This balance occurs when the fluid compressiblity is much smaller than the pore compressibility, such that pore and total compressibilities are approximately equal. Pore compressibility is influenced by pore geometry as well as porosity and matrix elastic properties and there is hence considerable variability and uncertainty. This speaks to the need for experimental constraints on pore compressibility at relevant pressure and temperature conditions, as well as geologic constraints on the lithology and pore structure of the rocks hosting slip.

Without large permeability changes, large-scale fluid flux is fairly steady despite rather large pressure changes ($\sim$1 to 10 MPa). Fluid flux does change by an order of magnitude, and can even reverse direction, but these changes are transient and localized to a few hundred meters behind advancing slip fronts. Our model is therefore rather different from the Zhu et al. (2020) model, in which permeability and hence fluid flux vary by many orders of magnitude in earthquake cycles that are modulated by fault valving. Large permeability changes occur because permeability was evolved with porosity held fixed, which is appropriate when permeability changes are driven by the evolution of tortuosity and pore connectivity rather than through changes in porosity. Slow slip events occur in both models, but through different mechanisms. In our present study, SSEs are triggered by weakening from compaction-driven pressurization and velocity-weakening friction, with slip acceleration stalled by dilatant suctions. In contrast, SSEs in the Zhu et al. (2020) model are driven by the ascent of fluid overpressure pulses.

SSEs in both models occur at the base of the seismogenic zone, below the locking depth where most models neglecting fluid coupling would predict fairly steady sliding at the loading rate. However, the combination of fluid coupling and velocity-weakening friction presumably destabilizes the steady sliding solution, with the slip instabilities taking the form of SSEs. A testable prediction of the models is that successive SSEs incrementally raise the locking depth, which might be seen geodetically as a gradual unlocking of the seismogenic zone (Mavrommatis et al., 2014; Bruhat & Segall, 2017). Seafloor geodetic observations are probably required to provide sufficient spatial resolution of these processes (Bürgmann & Chadwell, 2014).

We also note that in our model and the Zhu et al. (2020) model, SSEs occur where effective normal stress is approximately 20 to 30 MPa. This is higher than in most models for slow slip, which appeal to effective normal stresses of $\sim$0.1–1 MPa. We have not explored the sensitivity of SSEs in our model to tidal body forces, but note that the observed sensitivity of SSEs and tremor to tides might provide a means to falsify both our model and the Zhu et al. (2020) model (or at least motivate the exploration of other parameter choices in those models).

An improvement to our model, which would serve to decrease the effective normal stress, is to account for the reduction in total normal stress acting on the fault in response to dislocation creep and similar flow mechanisms in the bulk surrounding the fault. That flow acts to equilibrate all three principal stresses with lithostatic pressure, and then creep closure of pores would raise pore pressure toward lithostatic. Earthquake sequence models in viscoelastic solids have been developed (Lambert & Barbot, 2016; Allison & Dunham, 2018; Dal Zilio, Lapusta, et al., 2022; Dal Zilio, Hegyi, et al., 2022), so the next step is to integrate bulk viscoelasticity with fault zone fluid flow. We note that the model of Dal Zilio, Hegyi, et al. (2022) and Dal Zilio and Gerya (2022) does this, but with slip on a frictional interface replaced with distributed plastic strain in a finite width shear zone. To capture frictional weakening, the effective shear viscosity within this shear zone is reduced by many orders of magnitude. The same shear viscosity is used to set the effective bulk viscosity that governs creep compaction of pores. This leads to coseismic compaction and weakening from pressurization. In contrast, our model utilizes a bulk viscosity that remains relatively constant during earthquakes and SSEs, such that compaction occurs only over much longer time scales. We argue that this is a more appropriate description when slip is localized. Clearly more work is required to assess the validity of these very different models for compaction and its role in earthquake and slip dynamics.

Experimental, geochemical, and geologic constraints will also be essential for distinguishing among models. Both laboratory and field experiments (Guglielmi et al., 2015; Ishibashi et al., 2018; Im et al., 2019) show evidence for permeability enhancement by slip, but are generally conducted at pressures and temperatures much lower than those at the depth of slow earthquakes. Geologic studies provide evidence for cyclic changes in pore pressure in the form of mineral-filled veins and crack-seal features (Sibson, 1992b, 2000; Cox, 2005, 2010; Sibson, 2017, 2020). Constraints from geochemistry are needed to ascertain the source of silica and other precipitated minerals that fill the veins, in particular if those minerals are sourced locally or require transport from greater depths by ascending fluids (Williams & Fagereng, 2022). Lithium isotope geochemistry appears promising for resolving the short time scales of earthquake cycles (Penniston-Dorland et al., 2017) and provides evidence for transient fluid flow events in eclogite-facies subduction rocks from slow earthquake depths (Hoover et al., 2022). These studies speak to the need for future modeling efforts to more explicitly account for dissolution, transport, and precipitation of silica and other minerals, in addition to fluid flow and pressure dynamics. Given the strong temperature dependence of reaction kinetics, these models should also account for shear heating and heat transport by conduction and advection.

7 Conclusion

We have introduced an earthquake sequence model for a vertical strike-slip fault in a linear elastic solid with fault zone fluid transport and pore pressure diffusion. We account for elastic, viscous, and plastic porosity evolution within the fault zone, with permeability having a power-law dependence on porosity. The model produces large earthquakes in the seismogenic zone, whose recurrence interval is controlled in part by compaction-driven pressurization and weakening. The model also produces a complex sequence of slow slip events at the base of the seismogenic zone. The SSEs are driven by the interaction between pore compaction which raises fluid pressure and weakens the fault, as well as pore dilation which decreases fluid pressure and limits the slip instability. The cyclic behaviors exhibited by the SSEs can range from long-term events lasting from a few months to years, to very rapid short-term events lasting for only a few days. The accumulated slip for each event is on the order of centimeters. Our model demonstrates the important role that compaction and dilatancy have on fluid pressure and fault slip. While the modeling is conducted for a vertical strike-slip fault, the processes and behaviors are most likely relevant across a range of tectonic environments, including subduction zones. Extending these models to subduction zones, where fluid production rates and fluxes are generally much higher than for faults in continental crust, is an important next step.

8 Open Research

The earthquake sequence modeling code, simulation input and output files are available at `https://doi.org/10.17605/OSF.IO/X7HSW`. Figure 1 is modified from Zhu et al. (2020) under the Creative Commons license `http://creativecommons.org/licenses/by/4.0/`.

Acknowledgments

This work was funded by the National Science Foundation (EAR-1947448) and US Geological Survey (G21AP10026). We thank Weiqiang Zhu for assistance with problem setup and comments.

References

Allison, K. L., & Dunham, E. M. (2018). Earthquake cycle simulations with rate-and-state friction and power-law viscoelasticity. *Tectonophysics*, *733*, 232–256. doi: 10.1016/j.tecto.2017.10.021

Andrews, D. (2005). Rupture dynamics with energy loss outside the slip zone. *Journal of Geophysical Research: Solid Earth*, *110*(B1). doi: 10.1029/2004JB003191

Araki, E., Saffer, D. M., Kopf, A. J., Wallace, L. M., Kimura, T., Machida, Y., ... others (2017). Recurring and triggered slow-slip events near the trench at the Nankai Trough subduction megathrust. *Science*, *356*(6343), 1157–1160. doi: 10.1126/science.aan3120

Audet, P., Bostock, M. G., Christensen, N. I., & Peacock, S. M. (2009). Seismic evidence for overpressured subducted oceanic crust and megathrust fault sealing. *Nature*, *457*(7225), 76–78. doi: 10.1038/nature07650

Behr, W. M., & Bürgmann, R. (2021). What's down there? The structures, materials and environment of deep-seated slow slip and tremor. *Philosophical Transactions of the Royal Society A*, *379*(2193), 20200218. doi: 10.1098/rsta.2020.0218

Beroza, G. C., & Ide, S. (2011). Slow earthquakes and nonvolcanic tremor. *Annual review of Earth and planetary sciences*, *39*, 271–296. doi: 10.1146/annurev-earth-040809-152531

Brace, W., & Kohlstedt, D. (1980). Limits on lithospheric stress imposed by laboratory experiments. *Journal of Geophysical Research: Solid Earth*, *85*(B11), 6248–6252. doi: 10.1029/JB085iB11p06248

Brantut, N. (2020). Dilatancy-induced fluid pressure drop during dynamic rupture: Direct experimental evidence and consequences for earthquake dynamics. *Earth and Planetary Science Letters*, *538*, 116179. doi: 10.1016/j.epsl.2020.116179

Bruhat, L., & Segall, P. (2017). Deformation rates in northern Cascadia consistent with slow updip propagation of deep interseismic creep. *Geophysical Journal International*, *211*(1), 427–449. doi: doi.org/10.1093/gji/ggx317

Bürgmann, R. (2018). The geophysics, geology and mechanics of slow fault slip. *Earth and Planetary Science Letters*, *495*, 112–134. doi: 10.1016/j.epsl.2018.04.062

Bürgmann, R., & Chadwell, D. (2014). Seafloor geodesy. *Annual Review of Earth and Planetary Sciences*, *42*, 509–534. doi: 10.1146/annurev-earth-060313-054953

Byerlee, J. (1978). Friction of rocks. In *Rock friction and earthquake prediction* (pp. 615–626). doi: 10.1007/BF00876528

Caine, J. S., Evans, J. P., & Forster, C. B. (1996). Fault zone architecture and permeability structure. *Geology*, *24*(11), 1025–1028. doi: 10.1130/0091-7613(1996)024⟨1025:FZAAPS⟩2.3.CO;2

Cawood, T., & Platt, J. (2021). What controls the width of ductile shear zones? *Tectonophysics*, *816*, 229033. doi: 10.1016/j.tecto.2021.229033

Civan, F. (2001). Scale effect on porosity and permeability: Kinetics, model, and correlation. *AIChE journal*, *47*(2), 271–287. doi: 10.1002/aic.690470206

Cole, J., Hacker, B., Ratschbacher, L., Dolan, J., Seward, G., Frost, E., & Frank, W. (2007). Localized ductile shear below the seismogenic zone: Structural analysis of an exhumed strike-slip fault, Austrian Alps. *Journal of Geophysical Research: Solid Earth*, *112*(B12). doi: 10.1029/2007JB004975

Condit, C., & French, M. (2022). Geologic evidence of lithostatic pore fluid pressures at the base of the subduction seismogenic zone. *Geophysical Research Letters*, *49*(12), e2022GL098862. doi: 10.1029/2022GL098862

Condit, C., Guevara, V., Delph, J., & French, M. (2020). Slab dehydration in warm subduction zones at depths of episodic slip and tremor. *Earth and Planetary Science Letters*, *552*, 116601. doi: 10.1016/j.epsl.2020.116601

Cox, S. F. (2005). Coupling between deformation, fluid pressures, and fluid flow in ore-producing hydrothermal systems at depth in the crust. *Economic Geology; Bulletin of the Society of Economic Geologists*, *100*, 39–75.

Cox, S. F. (2010). The application of failure mode diagrams for exploring the roles of fluid pressure and stress states in controlling styles of fracture-controlled permeability enhancement in faults and shear zones. *Geofluids*, *10*(1-2), 217–233. doi: 10.1111/j.1468-8123.2010.00281.x

Dal Zilio, L., & Gerya, T. (2022). Subduction earthquake cycles controlled by episodic fluid pressure cycling. *Lithos*, *426*, 106800. doi: 10.1016/j.lithos.2022.106800

Dal Zilio, L., Hegyi, B., Behr, W., & Gerya, T. (2022). Hydro-mechanical earthquake cycles in a poro-visco-elasto-plastic fluid-bearing fault structure. *Tectonophysics*, *838*, 229516. doi: 10.1016/j.tecto.2022.229516

Dal Zilio, L., Lapusta, N., Avouac, J.-P., & Gerya, T. (2022). Subduction earthquake sequences in a non-linear visco-elasto-plastic megathrust. *Geophysical Journal International*, *229*(2), 1098–1121. doi: 10.1093/gji/ggab521

Dieterich, J. H. (1992). Earthquake nucleation on faults with rate-and state-dependent strength. *Tectonophysics*, *211*(1-4), 115–134. doi: 10.1016/0040-1951(92)90055-B

Duru, K., Allison, K. L., Rivet, M., & Dunham, E. M. (2019). Dynamic rupture and earthquake sequence simulations using the wave equation in second-order form. *Geophysical Journal International*, *219*(2), 796–815. doi: 10.1093/gji/ggz319

Erickson, B. A., & Dunham, E. M. (2014). An efficient numerical method for earthquake cycles in heterogeneous media: Alternating subbasin and surface-rupturing events on faults crossing a sedimentary basin. *Journal of Geophysical Research: Solid Earth*, *119*(4), 3290–3316. doi: 10.1002/2013JB010614

Erickson, B. A., Jiang, J., Lambert, V., Abdelmeguid, M., Almquist, M., Ampuero, J. P., … others (2022). *Incorporating full elastodynamic effects and dipping fault geometries in community code verification exercises for simulations of earthquake sequences and aseismic slip (SEAS).* (preprint available at doi:10.31223/X5NP87)

Fagereng, Å., & Diener, J. F. (2011). Non-volcanic tremor and discontinuous slab dehydration. *Geophysical Research Letters*, *38*(15). doi: 10.1029/2011GL048214

Fagereng, Å., & Toy, V. G. (2011). Geology of the earthquake source: an introduction. *Geological Society, London, Special Publications*, *359*(1), 1–16. doi: 10.1144/SP359.1

Faulkner, D., Jackson, C., Lunn, R., Schlische, R., Shipton, Z., Wibberley, C., & Withjack, M. (2010). A review of recent developments concerning the structure, mechanics and fluid flow properties of fault zones. *Journal of Structural Geology*, *32*(11), 1557–1575. doi: 10.1016/j.jsg.2010.06.009

Faulkner, D., & Rutter, E. (2001). Can the maintenance of overpressured fluids in large strike-slip fault zones explain their apparent weakness? *Geology*, *29*(6), 503–506. doi: 10.1130/0091-7613(2001)029⟨0503:CTMOOF⟩2.0.CO;2

Faulkner, D., Sanchez-Roa, C., Boulton, C., & Den Hartog, S. A. M. (2018). Pore fluid pressure development in compacting fault gouge in theory, experiments, and nature. *Journal of Geophysical Research: Solid Earth*, *123*(1), 226–241.

doi: 10.1002/2017JB015130

Fossen, H., & Cavalcante, G. C. G. (2017). Shear zones–a review. *Earth-Science Reviews*, *171*, 434–455. doi: 10.1016/j.earscirev.2017.05.002

Frank, W. B., Shapiro, N. M., Husker, A. L., Kostoglodov, V., Bhat, H. S., & Campillo, M. (2015). Along-fault pore-pressure evolution during a slow-slip event in Guerrero, Mexico. *Earth and Planetary Science Letters*, *413*, 135–143. doi: 10.1016/j.epsl.2014.12.051

Frost, E., Dolan, J., Ratschbacher, L., Hacker, B., & Seward, G. (2011). Direct observation of fault zone structure at the brittle-ductile transition along the Salzach-Ennstal-Mariazell-Puchberg fault system, Austrian Alps. *Journal of Geophysical Research: Solid Earth*, *116*(B2). doi: 10.1029/2010JB007719

Fulton, P. M., & Saffer, D. M. (2009). Potential role of mantle-derived fluids in weakening the San Andreas Fault. *Journal of Geophysical Research: Solid Earth*, *114*(B7). doi: 10.1029/2008JB006087

Ghanbarian, B., Hunt, A. G., Ewing, R. P., & Sahimi, M. (2013). Tortuosity in porous media: a critical review. *Soil science society of America journal*, *77*(5), 1461–1477. doi: 10.2136/sssaj2012.0435

Goetze, C., & Evans, B. (1979). Stress and temperature in the bending lithosphere as constrained by experimental rock mechanics. *Geophysical Journal International*, *59*(3), 463–478. doi: 10.1111/j.1365-246X.1979.tb02567.x

Gosselin, J. M., Audet, P., Estève, C., McLellan, M., Mosher, S. G., & Schaeffer, A. J. (2020). Seismic evidence for megathrust fault-valve behavior during episodic tremor and slip. *Science advances*, *6*(4), eaay5174. doi: 10.1126/sciadv.aay5174

Gratier, J.-P., Dysthe, D. K., & Renard, F. (2013). The role of pressure solution creep in the ductility of the Earth's upper crust. *Advances in geophysics*, *54*, 47–179. doi: 10.1016/B978-0-12-380940-7.00002-0

Gratier, J.-P., Favreau, P., & Renard, F. (2003). Modeling fluid transfer along California faults when integrating pressure solution crack sealing and compaction processes. *Journal of Geophysical Research: Solid Earth*, *108*(B2). doi: 10.1029/2001jb000380

Guglielmi, Y., Cappa, F., Avouac, J.-P., Henry, P., & Elsworth, D. (2015). Seismicity triggered by fluid injection–induced aseismic slip. *Science*, *348*(6240), 1224–1226. doi: 10.1126/science.aab0476

Guo, H., Brodsky, E., Goebel, T., & Cladouhos, T. (2021). Measuring fault zone and host rock hydraulic properties using tidal responses. *Geophysical Research Letters*, *48*(13), e2021GL093986. doi: 10.1029/2021GL093986

Hacker, B. R., Peacock, S. M., Abers, G. A., & Holloway, S. D. (2003). Subduction factory 2. are intermediate-depth earthquakes in subducting slabs linked to metamorphic dehydration reactions? *Journal of Geophysical Research: Solid Earth*, *108*(B1). doi: 10.1029/2001JB001129

Hickman, S., Sibson, R. H., & Bruhn, R. (1995). *Introduction to special section: Mechanical involvement of fluids in faulting* (Vol. 100) (No. B7). doi: 10.1029/95JB01121

Hirose, H., & Obara, K. (2005). Repeating short-and long-term slow slip events with deep tremor activity around the Bungo channel region, southwest Japan. *Earth, planets and space*, *57*(10), 961–972. doi: 10.1186/BF03351875

Hoover, W. F., Penniston-Dorland, S., Baumgartner, L., Bouvier, A.-S., Dragovic, B., Locatelli, M., ... Agard, P. (2022). Episodic fluid flow in an eclogite-facies shear zone: Insights from Li isotope zoning in garnet. *Geology*, *50*(6), 746–750. doi: 10.1130/G49737.1

Hughes, C. A., Jessup, M. J., Shaw, C. A., & Newell, D. L. (2020). Evidence for strain rate variation and an elevated transient geothermal gradient during shear zone evolution in the Cordillera Blanca, Peru. *Tectonophysics*, *794*, 228610. doi: 10.1016/j.tecto.2020.228610

Hyndman, R. D., & Peacock, S. M. (2003). Serpentinization of the forearc mantle. *Earth and Planetary Science Letters*, *212*(3-4), 417–432. doi: 10.1016/S0012-821X(03)00263-2

Im, K., Elsworth, D., & Fang, Y. (2018). The influence of preslip sealing on the permeability evolution of fractures and faults. *Geophysical Research Letters*, *45*(1), 166–175.

Im, K., Elsworth, D., & Wang, C. (2019). Cyclic permeability evolution during repose then reactivation of fractures and faults. *Journal of Geophysical Research: Solid Earth*, *124*(5), 4492–4506. doi: 10.1029/2019JB017309

Ishibashi, T., Elsworth, D., Fang, Y., Riviere, J., Madara, B., Asanuma, H., ... Marone, C. (2018). Friction-stability-permeability evolution of a fracture in granite. *Water Resources Research*, *54*(12), 9901–9918. doi: 10.1029/2018WR022598

Ito, Y., Obara, K., Shiomi, K., Sekine, S., & Hirose, H. (2007). Slow earthquakes coincident with episodic tremors and slow slip events. *Science*, *315*(5811), 503–506. doi: 10.1126/science.1134454

Jolivet, R., & Frank, W. (2020). The transient and intermittent nature of slow slip. *AGU Advances*, *1*(1), e2019AV000126. doi: 10.1029/2019AV000126

Karato, S. (2008). Deformation of earth materials. *An Introduction to the Rheology of Solid Earth*, *463*.

Kennedy, B., Kharaka, Y., Evans, W. C., Ellwood, A., DePaolo, D., Thordsen, J., ... Mariner, R. (1997). Mantle fluids in the San Andreas Fault system, California. *Science*, *278*(5341), 1278–1281. doi: 10.1126/science.278.5341.1278

Kerrick, D., & Connolly, J. (2001). Metamorphic devolatilization of subducted marine sediments and the transport of volatiles into the Earth's mantle. *Nature*, *411*(6835), 293–296. doi: 10.1038/35077056

Khoshmanesh, M., & Shirzaei, M. (2018). Episodic creep events on the San Andreas Fault caused by pore pressure variations. *Nature geoscience*, *11*(8), 610–614. doi: 10.1038/s41561-018-0160-2

Kim, Y.-S., Peacock, D. C., & Sanderson, D. J. (2004). Fault damage zones. *Journal of structural geology*, *26*(3), 503–517. doi: 10.1016/j.jsg.2003.08.002

Kirkpatrick, J. D., Fagereng, Å., & Shelly, D. R. (2021). Geological constraints on the mechanisms of slow earthquakes. *Nature Reviews Earth & Environment*, *2*(4), 285–301. doi: 10.1038/s43017-021-00148-w

Kirkpatrick, J. D., & Rowe, C. D. (2013). Disappearing ink: How pseudotachylytes are lost from the rock record. *Journal of Structural Geology*, *52*, 183–198. doi: 10.1016/j.jsg.2013.03.003

Klein, E., Duputel, Z., Zigone, D., Vigny, C., Boy, J.-P., Doubre, C., & Meneses, G. (2018). Deep transient slow slip detected by survey GPS in the region of Atacama, Chile. *Geophysical research letters*, *45*(22), 12–263. doi: 10.1029/2018GL080613

Kobayashi, A. (2017). Objective detection of long-term slow slip events along the Nankai Trough using GNSS data (1996–2016). *Earth, Planets and Space*, *69*(1), 1–12. doi: 10.1186/s40623-017-0755-7

Lambert, V., & Barbot, S. (2016). Contribution of viscoelastic flow in earthquake cycles within the lithosphere-asthenosphere system. *Geophysical Research Letters*, *43*(19), 10–142. doi: 10.1002/2016GL070345

Liu, Y., & Rubin, A. M. (2010). Role of fault gouge dilatancy on aseismic deformation transients. *Journal of Geophysical Research: Solid Earth*, *115*(B10414). doi: 10.1029/2010JB007522

Lockner, D. A., & Byerlee, J. D. (1994). Dilatancy in hydraulically isolated faults and the suppression of instability. *Geophysical Research Letters*, *21*(22), 2353–2356. doi: 10.1029/94GL02366

Marone, C. (1998). Laboratory-derived friction laws and their application to seismic faulting. *Annual Review of Earth and Planetary Sciences*, *26*(1), 643–696. doi:

10.1146/annurev.earth.26.1.643
Marone, C., Raleigh, C. B., & Scholz, C. (1990). Frictional behavior and constitutive modeling of simulated fault gouge. *Journal of Geophysical Research: Solid Earth*, *95*(B5), 7007–7025. doi: 10.1029/JB095iB05p07007
Matsuzawa, T., Hirose, H., Shibazaki, B., & Obara, K. (2010). Modeling short- and long-term slow slip events in the seismic cycles of large subduction earthquakes. *Journal of Geophysical Research: Solid Earth*, *115*(B12). doi: 10.1029/2010JB007566
Matyka, M., Khalili, A., & Koza, Z. (2008). Tortuosity-porosity relation in porous media flow. *Physical Review E*, *78*(2), 026306. doi: 10.1103/PhysRevE.78.026306
Mavko, G., Mukerji, T., & Dvorkin, J. (2020). *The rock physics handbook*. Cambridge university press.
Mavrommatis, A. P., Segall, P., & Johnson, K. M. (2014). A decadal-scale deformation transient prior to the 2011 Mw 9.0 Tohoku-oki earthquake. *Geophysical Research Letters*, *41*(13), 4486–4494. doi: 10.1002/2014GL060139
McGrath, A. G., & Davison, I. (1995). Damage zone geometry around fault tips. *Journal of Structural Geology*, *17*(7), 1011–1024. doi: 10.1016/0191-8141(94)00116-H
Menegon, L., & Fagereng, Å. (2021). Tectonic pressure gradients during viscous creep drive fluid flow and brittle failure at the base of the seismogenic zone. *Geology*, *49*(10), 1255–1259. doi: 10.1130/G49012.1
Menzies, C. D., Teagle, D. A., Niedermann, S., Cox, S. C., Craw, D., Zimmer, M., ... Erzinger, J. (2016). The fluid budget of a continental plate boundary fault: Quantification from the Alpine Fault, New Zealand. *Earth and Planetary Science Letters*, *445*, 125–135. doi: 10.1016/j.epsl.2016.03.046
Miller, S. A., & Nur, A. (2000). Permeability as a toggle switch in fluid-controlled crustal processes. *Earth and Planetary Science Letters*, *183*(1-2), 133–146. doi: 10.1016/S0012-821X(00)00263-6
Miller, S. A., Nur, A., & Olgaard, D. L. (1996). Earthquakes as a coupled shear stress-high pore pressure dynamical system. *Geophysical Research Letters*, *23*(2), 197–200. doi: 10.1029/95GL03178
Molnar, P., Anderson, H. J., Audoine, E., Eberhart-Phillips, D., Gledhill, K. R., Klosko, E. R., ... others (1999). Continuous deformation versus faulting through the continental lithosphere of New Zealand. *Science*, *286*(5439), 516–519. doi: 10.1126/science.286.5439.5
Morrow, C., Moore, D. E., & Lockner, D. (2001). Permeability reduction in granite under hydrothermal conditions. *Journal of Geophysical Research: Solid Earth*, *106*(B12), 30551–30560. doi: 10.1029/2000JB000010
Nelson, P. H. (1994). Permeability-porosity relationships in sedimentary rocks. *The Log Analyst*, *35*(03).
Norris, R. J., & Cooper, A. F. (2003). Very high strains recorded in mylonites along the Alpine Fault, New Zealand: implications for the deep structure of plate boundary faults. *Journal of Structural Geology*, *25*(12), 2141–2157. doi: 10.1016/S0191-8141(03)00045-2
Nur, A., & Walder, J. (1992). Hydraulic pulses in the Earth's crust. In *International geophysics* (Vol. 51, pp. 461–473). doi: 10.1016/S0074-6142(08)62834-X
Peacock, S. M. (2009). Thermal and metamorphic environment of subduction zone episodic tremor and slip. *Journal of Geophysical Research: Solid Earth*, *114*(B8). doi: 10.1029/2008JB005978
Peacock, S. M., Christensen, N. I., Bostock, M. G., & Audet, P. (2011). High pore pressures and porosity at 35 km depth in the Cascadia subduction zone. *Geology*, *39*(5), 471–474. doi: 10.1130/G31649.1
Peng, Z., & Gomberg, J. (2010). An integrated perspective of the continuum between earthquakes and slow-slip phenomena. *Nature geoscience*, *3*(9), 599–607.

doi: 10.1038/ngeo940
Penniston-Dorland, S., Liu, X.-M., & Rudnick, R. L. (2017). Lithium isotope geochemistry. *Reviews in Mineralogy and Geochemistry*, *82*(1), 165–217. doi: 10.2138/rmg.2017.82.6
Petrini, C., Gerya, T., Yarushina, V., van Dinther, Y., Connolly, J., & Madonna, C. (2020). Seismo-hydro-mechanical modelling of the seismic cycle: Methodology and implications for subduction zone seismicity. *Tectonophysics*, *791*, 228504. doi: 10.1016/j.tecto.2020.228504
Poirier, J.-P. (1985). *Creep of crystals: high-temperature deformation processes in metals, ceramics and minerals.* Cambridge University Press. doi: 10.1017/CBO9780511564451
Pritchard, M. E., Allen, R. M., Becker, T. W., Behn, M. D., Brodsky, E. E., Bürgmann, R., ... others (2020). New opportunities to study earthquake precursors. *Seismological Research Letters*, *91*(5), 2444–2447. doi: 10.1785/0220200089
Proctor, B., Lockner, D. A., Kilgore, B. D., Mitchell, T. M., & Beeler, N. M. (2020). Direct evidence for fluid pressure, dilatancy, and compaction affecting slip in isolated faults. *Geophysical Research Letters*, e2019GL086767. doi: 10.1029/2019GL086767
Radiguet, M., Cotton, F., Vergnolle, M., Campillo, M., Valette, B., Kostoglodov, V., & Cotte, N. (2011). Spatial and temporal evolution of a long term slow slip event: the 2006 Guerrero slow slip event. *Geophysical Journal International*, *184*(2), 816–828. doi: 10.1111/j.1365-246X.2010.04866.x
Renard, F., Gratier, J.-P., & Jamtveit, B. (2000). Kinetics of crack-sealing, intergranular pressure solution, and compaction around active faults. *Journal of Structural Geology*, *22*(10), 1395–1407. doi: 10.1016/S0191-8141(00)00064-X
Rice, J. R. (1992). Fault stress states, pore pressure distributions, and the weakness of the San Andreas fault. In *International geophysics* (Vol. 51, pp. 475–503). doi: 10.1016/S0074-6142(08)62835-1
Rice, J. R. (1993). Spatio-temporal complexity of slip on a fault. *Journal of Geophysical Research: Solid Earth*, *98*(B6), 9885–9907. doi: 10.1029/93JB00191
Rice, J. R. (2006). Heating and weakening of faults during earthquake slip. *Journal of Geophysical Research: Solid Earth*, *111*(B5). doi: 10.1029/2005JB004006
Rice, J. R., Lapusta, N., & Ranjith, K. (2001). Rate and state dependent friction and the stability of sliding between elastically deformable solids. *Journal of the Mechanics and Physics of Solids*, *49*(9), 1865–1898. doi: 10.1016/S0022-5096(01)00042-4
Rousset, B., Bürgmann, R., & Campillo, M. (2019). Slow slip events in the roots of the San Andreas Fault. *Science advances*, *5*(2), eaav3274. doi: 10.1126/sciadv.aav3274
Rubin, A. M., & Ampuero, J.-P. (2005). Earthquake nucleation on (aging) rate and state faults. *Journal of Geophysical Research: Solid Earth*, *110*(B11). doi: 10.1029/2005JB003686
Ruina, A. (1983). Slip instability and state variable friction laws. *Journal of Geophysical Research: Solid Earth*, *88*(B12), 10359–10370. doi: 10.1029/JB088iB12p10359
Ruiz, S., & Madariaga, R. (2018). Historical and recent large megathrust earthquakes in Chile. *Tectonophysics*, *733*, 37–56. doi: 10.1016/j.tecto.2018.01.015
Rutqvist, J., Wu, Y.-S., Tsang, C.-F., & Bodvarsson, G. (2002). A modeling approach for analysis of coupled multiphase fluid flow, heat transfer, and deformation in fractured porous rock. *International Journal of Rock Mechanics and Mining Sciences*, *39*(4), 429–442. doi: 10.1016/S1365-1609(02)00022-9
Rutter, E. (1983). Pressure solution in nature, theory and experiment. *Journal of the Geological Society*, *140*(5), 725–740. doi: 10.1144/gsjgs.140.5.072
Saffer, D. M., & Bekins, B. A. (1998). Episodic fluid flow in the Nankai accre-

tionary complex: Timescale, geochemistry, flow rates, and fluid budget. *Journal of Geophysical Research: Solid Earth*, *103*(B12), 30351–30370. doi: 10.1029/98jb01983

Saffer, D. M., & Tobin, H. J. (2011). Hydrogeology and mechanics of subduction zone forearcs: Fluid flow and pore pressure. *Annual Review of Earth and Planetary Sciences*, *39*, 157–186. doi: 10.1146/annurev-earth-040610-133408

Saffer, D. M., & Wallace, L. M. (2015). The frictional, hydrologic, metamorphic and thermal habitat of shallow slow earthquakes. *Nature Geoscience*, *8*(8), 594–600. doi: 10.1038/ngeo2490

Saishu, H., Okamoto, A., & Otsubo, M. (2017). Silica precipitation potentially controls earthquake recurrence in seismogenic zones. *Scientific reports*, *7*(1), 1–10. doi: 10.1038/s41598-017-13597-5

Samuelson, J., Elsworth, D., & Marone, C. (2009). Shear-induced dilatancy of fluid-saturated faults: Experiment and theory. *Journal of Geophysical Research: Solid Earth*, *114*(B12). doi: 10.1029/2008JB006273

Schmidt, W. L., & Platt, J. P. (2022). Stress, microstructure, and deformation mechanisms during subduction underplating at the depth of tremor and slow slip, Franciscan Complex, northern California. *Journal of Structural Geology*, *154*, 104469. doi: 10.1016/j.jsg.2021.104469

Schulz, R., Ray, N., Zech, S., Rupp, A., & Knabner, P. (2019). Beyond Kozeny–Carman: predicting the permeability in porous media. *Transport in Porous Media*, *130*(2), 487–512. doi: 10.1007/s11242-019-01321-y

Schwartz, S. Y., & Rokosky, J. M. (2007). Slow slip events and seismic tremor at circum-Pacific subduction zones. *Reviews of Geophysics*, *45*(3). doi: 10.1029/2006RG000208

Segall, P., & Bradley, A. M. (2012). Slow-slip evolves into megathrust earthquakes in 2D numerical simulations. *Geophysical Research Letters*, *39*(18). doi: 10.1029/2012GL052811

Segall, P., & Rice, J. R. (1995). Dilatancy, compaction, and slip instability of a fluid-infiltrated fault. *Journal of Geophysical Research: Solid Earth*, *100*(B11), 22155–22171. doi: 10.1029/95JB02403

Segall, P., Rubin, A. M., Bradley, A. M., & Rice, J. R. (2010). Dilatant strengthening as a mechanism for slow slip events. *Journal of Geophysical Research: Solid Earth*, *115*(B12). doi: 10.1029/2010JB007449

Shelly, D. R., & Hardebeck, J. L. (2010). Precise tremor source locations and amplitude variations along the lower-crustal central San Andreas Fault. *Geophysical Research Letters*, *37*(14). doi: 10.1029/2010GL043672

Sibson, R. H. (1983). Continental fault structure and the shallow earthquake source. *Journal of the Geological Society*, *140*(5), 741–767. doi: 10.1144/gsjgs.140.5.0741

Sibson, R. H. (1992a). Fault-valve behavior and the hydrostatic-lithostatic fluid pressure interface. *Earth-Science Reviews*, *32*(1-2), 141–144. doi: 10.1016/0012-8252(92)90019-P

Sibson, R. H. (1992b). Implications of fault-valve behaviour for rupture nucleation and recurrence. *Tectonophysics*, *211*(1-4), 283–293. doi: 10.1016/0040-1951(92)90065-E

Sibson, R. H. (2000). Fluid involvement in normal faulting. *Journal of Geodynamics*, *29*(3-5), 469–499. doi: 10.1016/S0264-3707(99)00042-3

Sibson, R. H. (2017). Tensile overpressure compartments on low-angle thrust faults. *Earth, Planets and Space*, *69*(1), 1–15. doi: 10.1186/s40623-017-0699-y

Sibson, R. H. (2020). Preparation zones for large crustal earthquakes consequent on fault-valve action. *Earth, Planets and Space*, *72*(1), 1–20. doi: 10.1186/s40623-020-01153-x

Skarbek, R. M., & Rempel, A. W. (2016). Dehydration-induced porosity waves and episodic tremor and slip. *Geochemistry, Geophysics, Geosystems*, *17*(2), 442–

469. doi: 10.1002/2015GC006155

Sleep, N. H., & Blanpied, M. L. (1992). Creep, compaction and the weak rheology of major faults. *Nature*, *359*(6397), 687–692. doi: 10.1038/359687a0

Sleep, N. H., & Blanpied, M. L. (1994). Ductile creep and compaction: A mechanism for transiently increasing fluid pressure in mostly sealed fault zones. *Pure and Applied Geophysics*, *143*(1), 9–40. doi: 10.1007/BF00874322

Suzuki, T., & Yamashita, T. (2009). Dynamic modeling of slow earthquakes based on thermoporoelastic effects and inelastic generation of pores. *Journal of Geophysical Research: Solid Earth*, *114*(B6). doi: 10.1029/2008JB006042

Templeton, E. L., & Rice, J. R. (2008). Off-fault plasticity and earthquake rupture dynamics: 1. Dry materials or neglect of fluid pressure changes. *Journal of Geophysical Research: Solid Earth*, *113*(B9). doi: 10.1029/2007JB005529

Ujiie, K., Saishu, H., Fagereng, Å., Nishiyama, N., Otsubo, M., Masuyama, H., & Kagi, H. (2018). An explanation of episodic tremor and slow slip constrained by crack-seal veins and viscous shear in subduction mélange. *Geophysical Research Letters*, *45*(11), 5371–5379. doi: 10.1029/2018GL078374

Viesca, R. C., Templeton, E. L., & Rice, J. R. (2008). Off-fault plasticity and earthquake rupture dynamics: 2. Effects of fluid saturation. *Journal of Geophysical Research: Solid Earth*, *113*(B9). doi: 10.1029/2007JB005530

Walder, J., & Nur, A. (1984). Porosity reduction and crustal pore pressure development. *Journal of Geophysical Research: Solid Earth*, *89*(B13), 11539–11548. doi: 10.1029/JB089iB13p11539

Wallace, L. M. (2020). Slow slip events in New Zealand. *Annual Review of Earth and Planetary Sciences*, *48*, 175–203. doi: 10.1146/annurev-earth-071719-055104

Wallace, L. M., Beavan, J., Bannister, S., & Williams, C. (2012). Simultaneous long-term and short-term slow slip events at the Hikurangi subduction margin, New Zealand: Implications for processes that control slow slip event occurrence, duration, and migration. *Journal of Geophysical Research: Solid Earth*, *117*(B11). doi: 10.1029/2012JB009489

Warren-Smith, E., Fry, B., Wallace, L., Chon, E., Henrys, S., Sheehan, A., ... Lebedev, S. (2019). Episodic stress and fluid pressure cycling in subducting oceanic crust during slow slip. *Nature Geoscience*, *12*(6), 475–481. doi: 10.1038/s41561-019-0367-x

Wibberley, C. A. (2002). Hydraulic diffusivity of fault gouge zones and implications for thermal pressurization during seismic slip. *Earth, Planets and Space*, *54*(11), 1153–1171. doi: 10.1186/BF03353317

Williams, R. T., & Fagereng, Å. (2022). The role of quartz cementation in the seismic cycle: a critical review. *Reviews of Geophysics*, *60*(1), e2021RG000768. doi: 10.1029/2021RG000768

Wood, D. M. (1990). *Soil behaviour and critical state soil mechanics.* Cambridge university press.

Woodcock, N., & Mort, K. (2008). Classification of fault breccias and related fault rocks. *Geological Magazine*, *145*(3), 435–440. doi: 10.1017/S0016756808004883

Xue, L., Brodsky, E. E., Erskine, J., Fulton, P. M., & Carter, R. (2016). A permeability and compliance contrast measured hydrogeologically on the San Andreas Fault. *Geochemistry, Geophysics, Geosystems*, *17*(3), 858–871. doi: 10.1002/2015GC006167

Xue, L., Li, H.-B., Brodsky, E. E., Xu, Z.-Q., Kano, Y., Wang, H., ... others (2013). Continuous permeability measurements record healing inside the Wenchuan earthquake fault zone. *Science*, *340*(6140), 1555–1559. doi: 10.1126/science.1237237

Yang, Y., & Dunham, E. M. (2021). Effect of porosity and permeability evolution on injection-induced aseismic slip. *Journal of Geophysical Research: Solid Earth*, *126*(7), e2020JB021258. doi: 10.1029/2020JB021258

Yarushina, V. M., Podladchikov, Y., & Wang, L. (2020). Model for (de) compaction and porosity waves in porous rocks under shear stresses. *Journal of Geophysical Research: Solid Earth*, *125*(8), e2020JB019683. doi: 10.1029/2020JB019683

Zhu, W., Allison, K. L., Dunham, E. M., & Yang, Y. (2020). Fault valving and pore pressure evolution in simulations of earthquake sequences and aseismic slip. *Nature communications*, *11*(1), 1–11. doi: 10.1038/s41467-020-18598-z

Zhu, W., David, C., & Wong, T. F. (1995). Network modeling of permeability evolution during cementation and hot isostatic pressing. *Journal of Geophysical Research: Solid Earth*, *100*(B8), 15451–15464. doi: 10.1029/95JB00958